CONTENT

EMG Instrumentation Modeling and Feature Processing Based on Discrete Wavelet Transform

Rasyida Shabihah Zukro Aini

Electrical Engineering, University of PGRI Adi Buana Surabaya

Corresponding author: rasyida@unipasby.ac.id

Abstract. Electromyography (EMG) instrumentation is essential in generating electrical signals from skeletal muscles. EMG sensors are helpful in various cases requiring the detection of human muscle contractions, neuromuscular disorders, and rehabilitation. EMG instrumentation is divided into two parts, namely, the analogue part and the digital part. The EMG instrumentation design comprises a digital-to-analog converter (DAC), instrumentation amplifier, filter, and analog-to-digital converter (ADC). Meanwhile, in digital signal processing adopting the Discrete Wavelet Transform (DWT) method, frequency analysis using DWT has proven superior. It is used in various research and has exceptionally detailed coefficient features for classifying neuromuscular disease signals. Therefore, this research aims to design analogue and digital EMG instrumentation and identify features in the form of detailed coefficients. The data used are two Physionet signals from the anterior tibialis body with myopathy and neuropathy disorders. The results obtained for EMG analogue instrumentation provide the expected results until they reach the filter component stage. The resulting signal forms a block in the filter component, different from the initial EMG signal. Meanwhile, the DWT decomposition results are of the Daubechies4 wavelet type with the highest level 17, which has a high detail coefficient at low frequencies, high dilation and the result of a mixture of neuropathy and myopathy EMG signals, or in other words, at low energies, this result is by the DWT theorem. Determining the efficiency of the DWT detailed coefficient feature requires further study with the same signal subject. The DWT features obtained can then be developed for various needs in EMG signal recognition.

ARTICLE INFO

Indonesian Applied Physics Letters

INTRODUCTION

Electromyography (EMG) instrumentation aims to obtain electrical signals generated from skeletal muscles and detected on the skin's surface. Generally, this EMG has a type of surface electrode (Merletti et al., 2009). EMG sensors have several vital functions, including detecting human muscle contractions, diagnosing peripheral nervous system diseases, detecting neuromuscular diseases, assessing low back pain, kinesiology, motor control disorders, and reviewing rehabilitation results. One rehabilitation that can be observed using EMG is asthma rehabilitation, especially in the respiratory muscles, with the help of a spirometer (Zukro Aini et al., 2020).

EMG instrumentation has a standard preparation, with several components consisting of amplifiers and filters. The amplitude of the signal obtained from Surface EMG is 0-10 mV (peak-peak) and the filter used also has a range of 1 Hz-1 kHz with a sampling frequency of 5 kHz. These two components are the basis of the electrodiagnostic system (Tankisi et al., 2020). In addition to these two components, EMG is also integrated into digital instrumentation. Digital instrumentation converts the EMG analogue signal generated from the amplifier into a digital signal using an analogue-to-digital (AD) converter.

The result of EMG instrumentation is an EMG signal. Just like ECG signals (Shabihah et al., 2023) and other bioelectrical signals, digital signal processing is performed to simplify the interpretation of EMG signals. Frequency analysis, usually obtained from the Fourier transform, is essential but has the disadvantage of frequency variation over time. The wavelet transform simultaneously analyses signals in both the time and frequency domains. In some EMG studies, DWT plays a role in evaluating muscle fatigue (Chowdhury et al., 2013), classification features for signals for neuromuscular diseases (Achmamad & Jbari, 2020), signal denoising of both signals and images (Zhang et al., 2005), (Rasyida Shabihah Zukro Aini & Ira Puspasari, 2023). DWT is a reliable solution for multi-resolution/multi-frequency representation.

Therefore, this research aims to design the best EMG instrumentation modelling and its parameters with signal analysis in discrete wavelet transform. In the future, the features in the form of detailed coefficient energy generated from signal decomposition can be developed to implement EMG signal analysis in various fields.

RESEARCH METHODOLOGY

EMG Signal

Generally, EMG consists of 2 input electrode leads processed in the differential amplifier section. So, due to the limited signal database available, it is assumed that the first signal is an EMG signal for myopathy disorder, and the second signal is an EMG signal for neuropathy disorder. The electromyography (EMG) signals used are in the form of the Physionet database as "Example of electromyography" measured from the Tibialis Anterior body part in different subjects for each disorder. The signals were stored in a file extension (.txt) with a recording length of 60 seconds using a sampling frequency of 4000 Hz and a 16-bit ADC.

Analog Circuit

In the analogue part, EMG instrumentation is designed in several stages: digital-to-analogue converter (DAC), instrumentation amplifier, filter, and analogue-to-digital converter (ADC). This section will explain the design of some of these stages.

1. DAC

A digital-to-analog converter (DAC) is used because the Physionet data has undergone an ADC process. Hence, it must be returned to the analogue domain to assume it as a body signal from the electrodes. According to the information from the Physionet, the ADC used was 16-bit, so a 16-bit DAC was also used. The type of DAC used is AD5766. AD5766 has a voltage output. In Figure 1, the input data in a file is contained in Vdac. At the same time, the output (Vout) is given an additional 100 pF capacitor as decoupling, AVdd, and AVss are positive and negative power supply voltages of 12 V, respectively. In the NO section, a sine signal of 0.5 mV amplitude with a frequency of 1000 Hz is input, this is done to act as a "dither" to the 5V offset. Dither is a signal added and summed with digital data before being sent to the DAC. Dither helps increase the resolution of the DAC.

.

Indonesian Applied Physics Letters
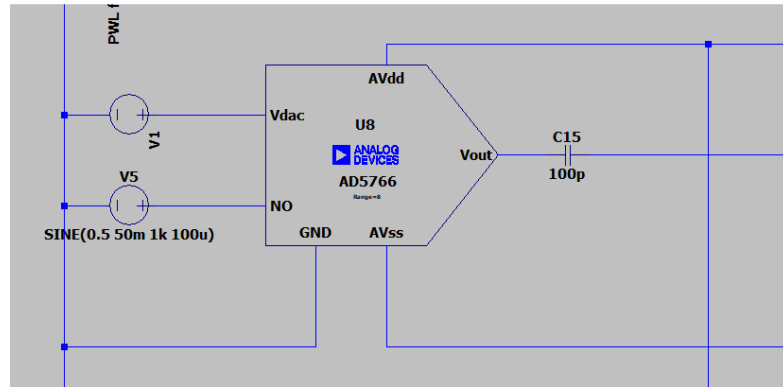
FIGURE 1. DAC 16 bit

2. Amplifier

Because the amplitude of the myopathy signal (V_1) that has been input to the DAC has a Vpp of 4.75 mV and the amplitude of the neuropathy signal (V_2) that has been input to the DAC has a Vpp of 10.5 mV and if the two are added together it will produce a Vpp of 5.75 mV, so there is no need for excessive gain, so an instrumentation amplifier is designed in Figure 2. Then, the gain of the result of Equation (1) should be around 0.83.

$$V_0 = \left(1 + 2\frac{49.9K}{100\,K}\right)\left(\frac{49.9K}{100\,K}\right)(10.5 - 4.75) = 4.78\ mV \tag{1}$$
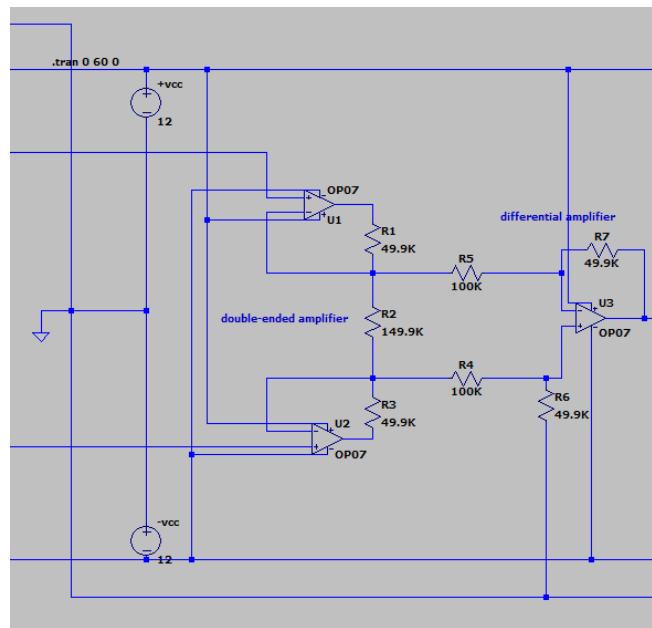
FIGURE 2. Instrumentation amplifier

Indonesian Applied Physics Letters
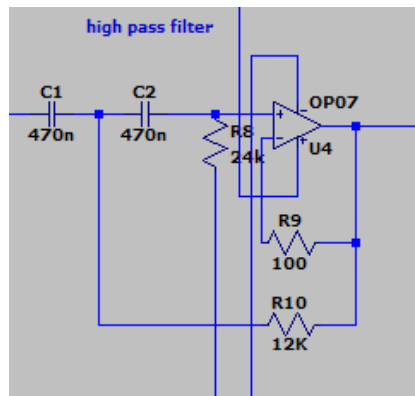
3. *Filter*

FIGURE 3. High Pass Filter -40 dB/dec

The filter has three stages: high pass filter, low pass filter and band pass filter. The high pass filter (HPF) design has a cut-off frequency of 20 Hz because the minimum frequency of normal EMG is 20 Hz. The HPF has a Sallen-Key topology Butterworth filter type of order 2 (Yuliansyah, 2017). This HPF circuit is used to reduce the signal below the frequency of 20 Hz.

From the condition of $\omega = \omega_c$ if the value of $C_1 = C_2 = C$ is made and the value of $R_{10} = 0.5R_8$, the calculation for connecting the cutoff frequency is shown in Equation (2)

$$f_c = \frac{1}{2\pi\sqrt{CCR_8 0.5R_8}} = \frac{1.414}{2\pi CR_8} \tag{2}$$

If the value of $C = 470nF$ is set, the value of R_8 is 24K and R_{10} is 12K, resulting in the HPF design in Figure 3
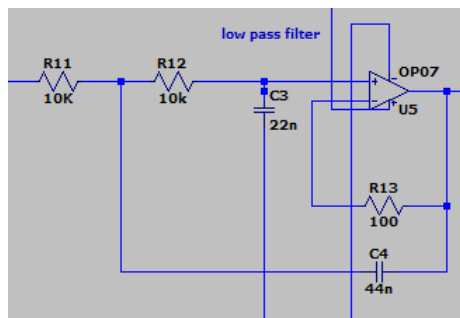
FIGURE 4. Low Pass Filter -40 dB/dec

Furthermore, the designed low pass filter (LPF) has a cut-off frequency of 500 Hz because the maximum frequency of normal EMG is 500 Hz. The LPF has a second-order Sallen-Key topology Butterworth filter type. This LPF circuit is used to avoid anti-aliasing when sampling.

From the condition $\omega = \omega_c$ if the value of $R_{11} = R_{12} = R$ and the value of $C_4 = 2C_2$ are made, the calculation for connecting the cutoff frequency is shown in Equation (3)

$$f_c = \frac{1}{2\pi\sqrt{C_3 2C_3 RR}} = \frac{0.707}{2\pi C_3 R} \tag{3}$$

If the value of $R = 10K$ is set, then the value of C_3 is 22 nF and C_4 is 47 nF (with the tolerance of components on the market), resulting in a design like Figure 4.

Indonesian Applied Physics Letters
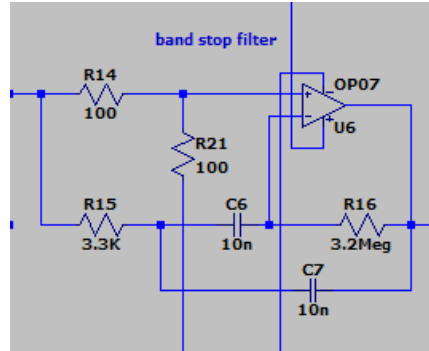
FIGURE 5. Band Stop Filter +40 dB/dec

The last stage in the analogue filter process is the Band stop filter (BSF), designed to have a cut-off frequency of 50 Hz, where there is interference from the mesh signal. In this design, the Q value is determined to be 5 to have a bandwidth that is not too narrow. Bandwidth can be found using Equation (4)

$$, B = \frac{\omega_c}{Q} = \frac{2\pi f_c}{Q} = \frac{2\pi 50}{5} = 62.8 \approx 63 \tag{4}$$

From the condition that $\omega = \omega r$ and the BSF gain drops to 0.707, the bandwidth is calculated according to Equation (5)

$$B = \frac{2}{R_2 C} \tag{5}$$

$$\omega_c = \frac{1}{C\sqrt{R_{15}R_{16}}} \tag{6}$$

If the value of $C_6 = C_7 = 10 \ nF$ is set, then the value of R_{16} if tolerated is 3.3M, then based on Equation (6) the value of R_{15} is 3.3k, resulting in a design like Figure 5.

4. ADC

The Analog Digital Converter (ADC) is an LTC 6360 Opamp. This component was chosen because it has low noise, high accuracy, and high speed. The power supply used is 5V (SHDN). The SAR ADC is designed with a non-inverting gain configuration. The input bias current induced DC voltage signal can be minimised using the parallel form of R_{17} and R_{18} to R_{20}. The relationship is calculated in Equations (7) and (8) resulting in the SAR ADC design in Figure 6.

$$\frac{R_{17}}{R_{18}} = \frac{V_{out}(\text{max}) - V_{out}(\text{min})}{V_{out}(\text{max}) - V_{out}(\text{min})} \tag{7}$$

$$V_3 = \frac{\left[\left(V_{out} + \frac{R_{17}}{R_{18}}\right) 2V_{in}\right]}{\left[1 + \frac{R_{17}}{R_{18}}\right]} \tag{8}$$

Indonesian Applied Physics Letters
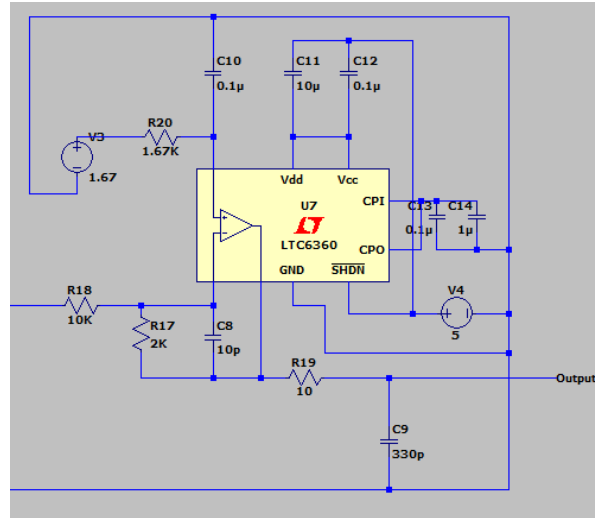
FIGURE 6. ADC 16 bit

Digital Signal Processing

In the digital part, EMG signal processing is divided into several stages: fast Fourier transform (FFT), Butterworth bandpass filter, and feature extraction in the form of detailed coefficient energy from discrete wavelet transform (DWT) decomposition. This section will explain the design of the EMG signal processing.

1. FFT

The FFT converts signals from the time domain to the frequency domain. The FFT is computed from the discrete Fourier transform (DFT). The FFT calculation is represented in Equation (9) where $x[n]$ is the EMG signal, n is the sample, and L is the amount of EMG signal data.

$$X[k] = \sum_{n=0}^{L-1} x[n]e^{-j2\pi/L}, \quad 0 \leq k \leq L-1 \tag{9}$$

2. Butterworth Bandpass Filter

After observing the frequency domain, since the frequency interval of an average EMG signal is between 20-500 Hz, a Butterworth bandpass filter was chosen because the signal from the EMG instrumentation is very different from the initial signal from the Physionet data.

3. Energy Coefficient Details

The steps in extracting detail coefficient energy features using DWT start by defining the wavelet parameters, namely the wavelet type and maximum level. The type of wavelet used is Daubechies4, while to determine the maximum level of decomposition, a calculation involving Equation (10) is used with the logic of thinking for the maximum level where at least one coefficient in the output is not disturbed by edge effects caused by signal extension. In other words, the decomposition stops when the signal becomes shorter than the length of the FIR filter for the given wavelet type.

$$\max level = \left| log_2 \left(\frac{data\ length}{filter\ length-1} \right) \right| \tag{10}$$

Next is the step of decomposing the signal into approximation and detail coefficients. The calculation for the decomposition process is presented in Equation (11).

$$W(l,s) = 2^{\frac{s}{2}} \sum_n x(n)\psi(2^s n - l) \tag{11}$$

Indonesian Applied Physics Letters

$$A(k) = \sum_n x(n)h(2k - n) \tag{12}$$

$$D(k) = \sum_n x(n)g(2k - n) \tag{13}$$

where l is shifting, s is scale, $x(n)$ is a discrete signal with signal sample parameters, and $\psi(n)$ is the mother wavelet. The decomposition result is the detail coefficient ($D(k)$) of the high pass filter and the approximation coefficient ($A(k)$) of the low pass filter. Meanwhile, $h(n)$ and $g(n)$ represent the half bands of the low and high pass, respectively. The last step is to determine the coefficient energy of each level with Equation (14) where N_1 is the length of the data.

$$E(D_k) = \sqrt{\frac{1}{N_1} \sum_{i=1}^{N_1} (D_k)^2[i]} \tag{14}$$

RESULT AND DISCUSSION

1. Analog

The errors of analogue instrumentation can be examined by comparing theoretical calculations and simulation results presented in this section; in addition, the EMG instrumentation will be tested to determine whether it is appropriate for the EMG signal. In addition, the EMG instrumentation will be tested to determine whether it is appropriate for the EMG signal.

2. DAC
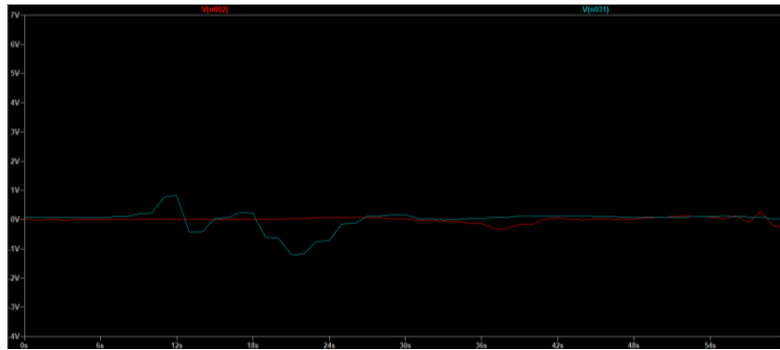
FIGURE 7. Raw signal 1 (red) and signal 2 (dark green)
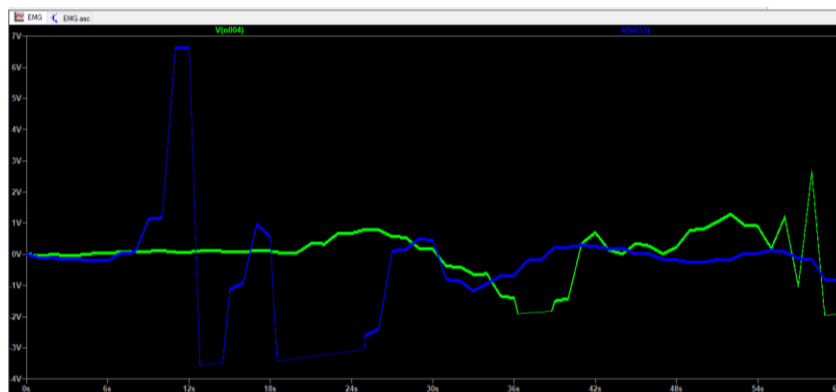
FIGURE 8. DAC signal 1 (green) and signal 2(blue)

From Figure 8, it is known that signal 1, which is the EMG signal of myopathy signal, produces a DAC with a Vpp amplitude of 4.75mV, while signal 2, which is a neuropathy EMG signal, produces a DAC with a Vpp amplitude of 10.5mV. Signal produces a DAC with a Vpp amplitude of 10.5 mV. The initial signal data (Figure 7) has experienced significant strengthening and shifting. Shifts are pretty significant. This is due to the effect of adding a sine signal as a dither that increases the signal amplitude by five mV.

a.   Amplifier Instrumentation
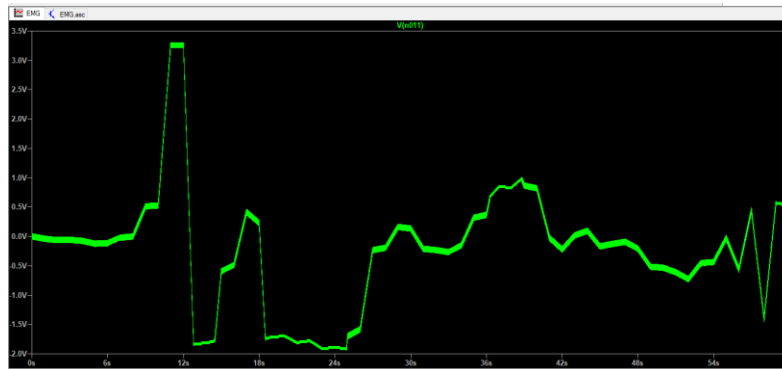
FIGURE 9. *Instrumentation amplifier* result

Figure 9 shows that the amplitude of the instrumentation amplifier results has a Vpp value of 5.35mV while Equation (1) has a Vpp value of 4.78mV. Results This result is different from the results of theoretical testing and simulation. In addition, the signal shape resembles a neuropathy signal due to its higher voltage, so the input in the differential amplifier still has a residual signal amplitude.

b.   Filter
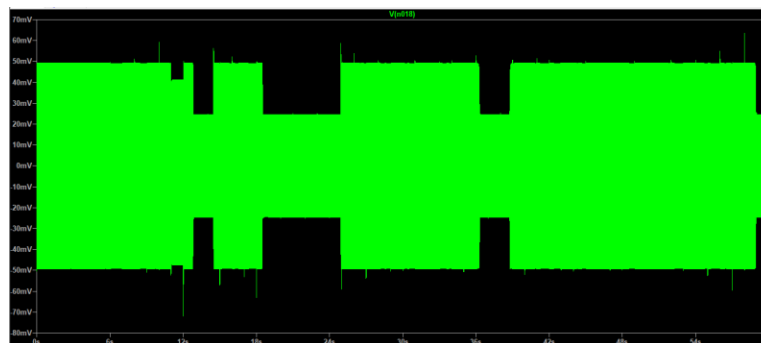
FIGURE 10. HPF -40 dB/dec with 20 Hz cutoff frequency

The result of the HPF at a cutoff frequency of 20 Hz (Figure 10) produces a signal block that is quite dense compared to the result of the instrumentation amplifier. It is pretty dense compared to the instrumentation amplifier results. The amplitude of this HPF result has a Vpp of 130 µV. The tentative hypothesis is the mismatch of the input signals that should have come from the same subject with adjacent areas and the same problem. Secondly, the HPF filter configuration does not match the signal characteristics.
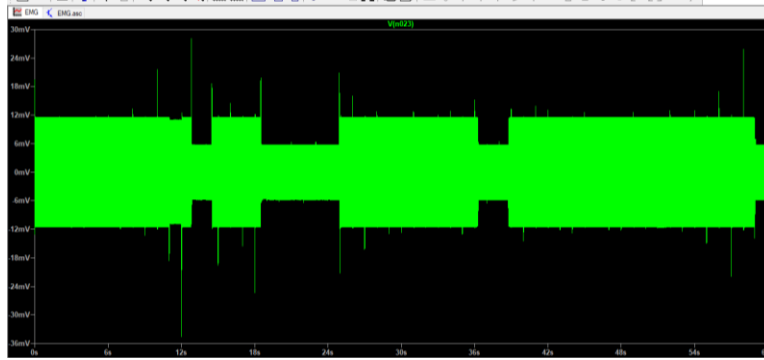
FIGURE 11. LPF -40 dB/dec with 500 Hz cutoff frequency

The result of the LPF at a cutoff frequency of 500 Hz (Figure 11) reduces the thickness of the signal block that occurs in Figure 16 but the signal's amplitude goes down to 63 µV. This explains the refutation of the second hypothesis. The EMG signal slowly starts to be visible.
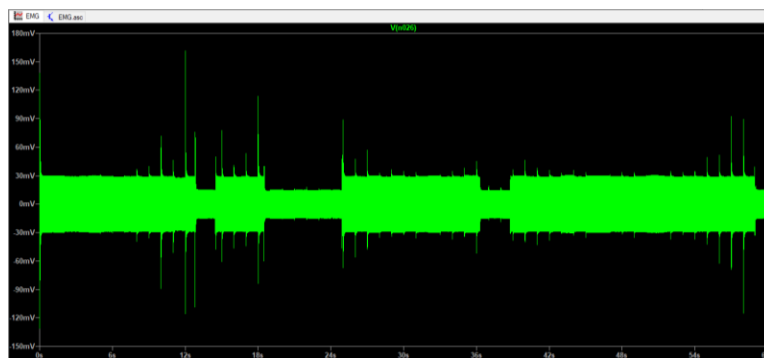
FIGURE 12. BSF +40 dB/dec with 50 Hz cutoff frequency

The result of BSF at a cutoff frequency of 50 Hz (Figure 12) to remove the mesh signal at a frequency of 50 Hz makes the EMG signal clearer. The signal at a frequency of 50 Hz further clarifies the EMG signal; this is also supported by the return of the EMG signal amplitude increase returns, whose Vpp is 285 µV. This explains the refutation of the second hypothesis. The EMG signal slowly began to be visible.

c.   ADC
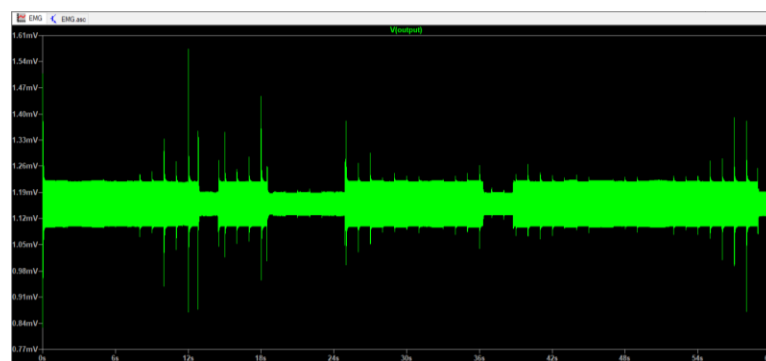
FIGURE 13. SAR ADC 16-bit result

When entering the value into Equation (7), the SAR ADC's results should produce an output signal Vpp of 57 µV, but the simulation results are much different; it only produces an output signal Vpp of 0.7 µV. The SAR ADC

Indonesian Applied Physics Letters

results also show a noise reduction, as evidenced by the more visible EMG signals. In addition, the signals are all above 0V or by the ADC configuration on the microcontroller, generally located between 0-5V.

3. *Digital*

The results of processing EMG signals in the digital domain will be discussed individually in this section to evaluate whether these results can be validated. Section to evaluate whether these results can be validated or not.

a. *FFT*
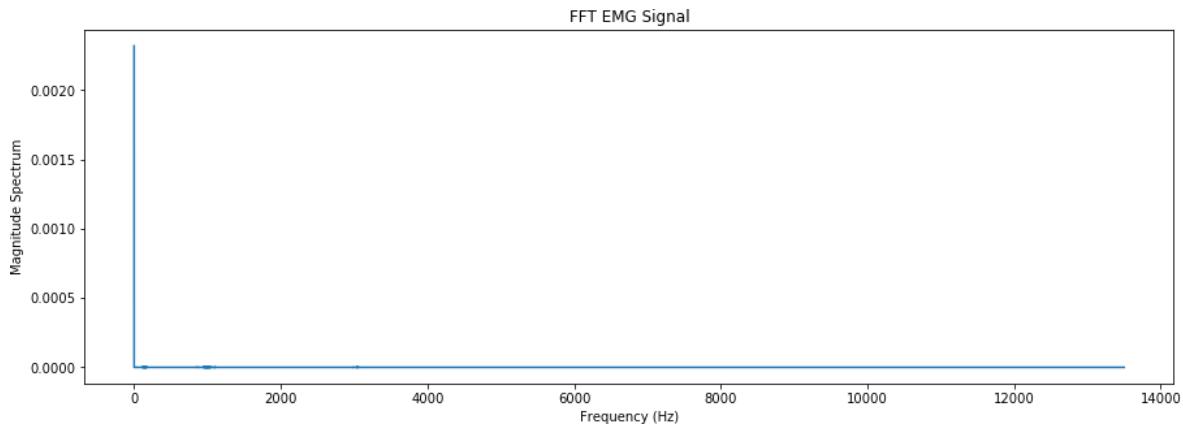
FIGURE 14. EMG signal FFT result

Based on the amount of data from analogue instrumentation results in 60 seconds, which reached 1.700.000 samples, it was decided to use a sampling frequency of 27.000, obtained by the number of samples divided by the length of the sampling time and obtained by the number of samples divided by the length of time sampling. Figure 14 shows several points at frequencies around 10 Hz, 1000 Hz, and 3000 Hz with a minimal magnitude spectrum. The magnitude spectrum is minimal.

b. *Butterworth Bandpass Filter*
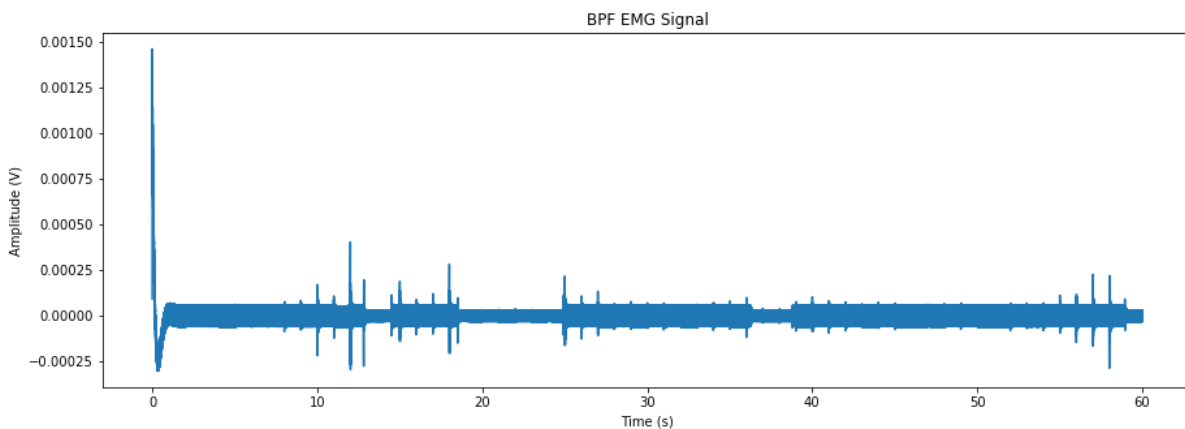
FIGURE 15. EMG signal BPF result

The FFT results are then applied to BPF signals with cutoff frequencies of 1 and 3001 Hz, obtained results as in Figure 15 with a signal amplitude of 0.5 µV.

c. *Energy Coefficient Details*

Indonesian Applied Physics Letters
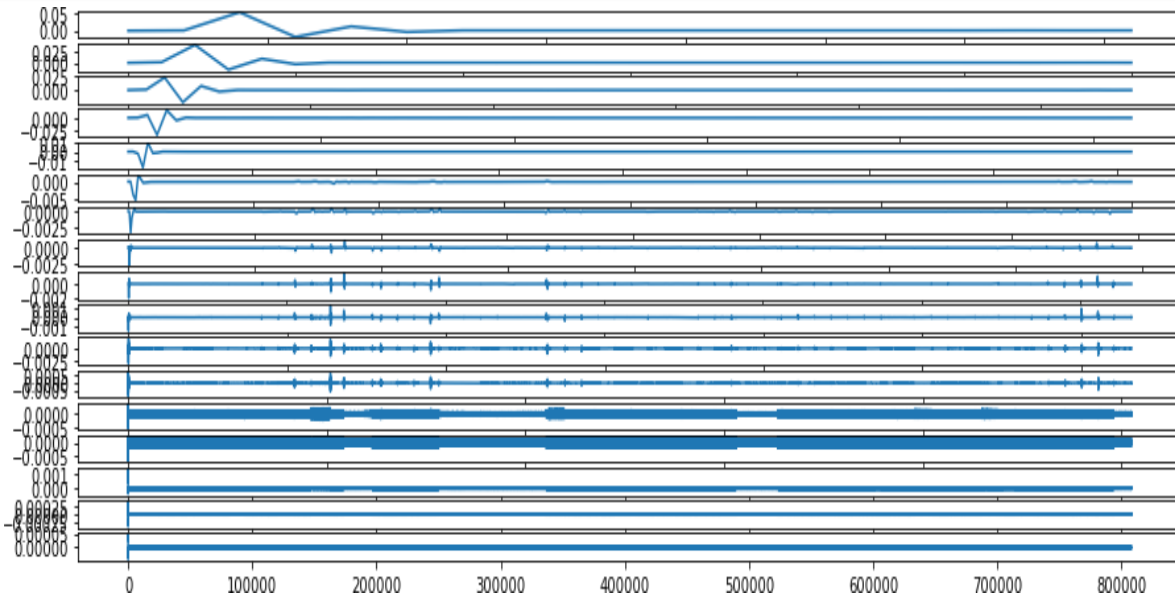
FIGURE 16. DWT Decomposition Result Coefficient

```
Energi  cD1 : 0.003175583166243954

Energi  cD2 : 0.0013979503981470767

Energi  cD3 : 0.0005965515914078321

Energi  cD4 : 0.00036055226156874224

Energi  cD5 : 9.947038978689109e-05

Energi  cD6 : 1.6997778928685936e-05

Energi  cD7 : 4.812742693448237e-06

Energi  cD8 : 2.2461244856390196e-06

Energi  cD9 : 1.2538211311289176e-06

Energi  cD10 :4.993712272649108e-07

Energi  cD11 :6.436510521814901e-07

Energi  cD12 :1.3388320258131966e-07

Energi  cD13 :3.81391435876562e-07

Energi  cD14 :3.714449366068671e-07

Energi  cD15 :4.5220322556479524e-08
```

Indonesian Applied Physics Letters

```
Energi  cD16 :7.273974850304083e-09

Energi  cD17 :4.5578972735573506e-10

Energi  cA17 :0.03181798188927217
```

The results of DWT decomposition using the Daubechies4 wavelet type at a maximum level of 17 show that the detail coefficients at higher levels are only found at low frequencies, and high dilation, and the results of mixing EMG neuropathy and myopathy signals produce energy in the cD1 to cD17 coefficients where the higher the level, the energy produced is also smaller. Smaller. For further research, this feature can be used to classify several signals into normal and abnormal data (Mustiadi et al., 2012).

CONCLUSION

The myopathy and neuropathy signals obtained from the anterior tibial body were from different subjects. The electromyography (EMG) instrumentation designed to process these two signals consists of a digital-to-analog converter (DAC), instrumentation amplifier, filter, and analog-to-digital converter (ADC). The DAC is adapted to the ADC originating from the database, namely 16-bit. As a result, both myopathy and neuropathy signals experienced a shift and strengthening of four times and three times the initial signal, respectively. There is no need to design excessive amplification because the amplitude of the myopathy signal is 4.75 mV, and the neuropathy signal is 10.5 mV, so a differential amplifier was designed. The differential amplifier output resembles a neuropathy signal and becomes input to three filters, namely the high pass filter (HPF), low pass filter (LPF), and band stop filter (BSF). The cut-off parameters given to HPF are 20 Hz, LPF is 500 Hz, and BPF is 50 Hz. These parameters are formed based on the minimum normal EMG frequency of 20 Hz and the maximum EMG frequency of 500 Hz. The overall combination of filters provides an overview of the EMG signal, but it is still in the form of blocks that do not match the initial signal; this is possible due to poor design in the filter instrumentation. Next, the ADC results follow the ADC configuration on the microcontroller. In digital signal processing, the DWT decomposition results are of the Daubechies4 wavelet type with the highest level 17, which has a high detail coefficient at low frequencies, high dilation and the result of a mixture of neuropathy and myopathy EMG signals, or in other words at low energies.

REFERENCES

1. Achmamad, A., & Jbari, A. (2020). A comparative study of wavelet families for electromyography signal classification based on discrete wavelet transform. *Bulletin of Electrical Engineering and Informatics*, *9*(4), 1420–1429. https://doi.org/10.11591/eei.v9i4.2381
2. Chowdhury, S. K., Nimbarte, A. D., Jaridi, M., & Creese, R. C. (2013). Discrete wavelet transform analysis of surface electromyography for the fatigue assessment of neck and shoulder muscles. *Journal of Electromyography and Kinesiology*, *23*(5), 995–1003. https://doi.org/10.1016/j.jelekin.2013.05.001
3. Merletti, R., Botter, A., Troiano, A., Merlo, E., & Minetto, M. A. (2009). Technology and instrumentation for detecting and conditioning the surface electromyographic signal: State of the art. *Clinical Biomechanics*, *24*(2), 122–134. https://doi.org/10.1016/j.clinbiomech.2008.08.006
4. Mustiadi, I., Widodo, T. S., & Soesanti, I. (2012). *Analisis Ekstraksi Ciri Sinyal Emgmenggunakan Wavelet Discrete Transform*. *2012*(semnasIF), 41–47.
5. Rasyida Shabihah Zukro Aini, & Ira Puspasari. (2023). Reliability of Radiomic Features Against Noise in the Use of Daubechies Wavelet Derived Features in Ct-Based Liver Tumor. In *BEST : Journal of Applied Electrical, Science, & Technology* (Vol. 5, Issue 1, pp. 33–38). https://doi.org/10.36456/best.vol5.no1.8026
6. Shabihah, R., Aini, Z., Sari, E., & Nurdiniyah, H. (2023). *Effectiveness of Wavelet and Fourier Transform Methods for Denoising ECG Apnea Signals*. *0*(02), 1–5.
7. Tankisi, H., Burke, D., Cui, L., de Carvalho, M., Kuwabara, S., Nandedkar, S. D., Rutkove, S., Stålberg, E., van Putten, M. J. A. M., & Fuglsang-Frederiksen, A. (2020). Standards of instrumentation of EMG. *Clinical*

Neurophysiology, *131*(1), 243–258. https://doi.org/10.1016/j.clinph.2019.07.025

8. Yuliansyah, D. (2017). Deteksi Kelelahan Otot Menggunakan Sinyal Emg Dan Detektor Gaya Pada Gerak Dasar Ekstensi Dan Fleksi Knee-Joint Untuk Evaluasi Penggunaan Functional Electrical Stimulation Pada Sistem Rehabilitasi Lower Limb. *Sepuluh Nopember Institute of Technology*, 171.

9. Zhang, J., Shou, G., & Dai, G. (2005). Denoising of ECG signals based on wavelet transform. *Xibei Gongye Daxue Xuebao/Journal of Northwestern Polytechnical University*, *23*(1), 11–14.

10. Zukro Aini, R. S., Arifin, A., & Babgei, A. F. (2020). Perancangan Mekanik Pulmonary Rehabilitation Robot sebagai Pendukung Mekanisme Rehabilitasi Asma Breathing Retraining. *Jurnal Teknik ITS*, *9*(1), 47–52. https://doi.org/10.12962/j23373539.v9i1.48237

The Implementation of Channel Area Thresholding in Early Detection System of Acute Respiratory Infection

Zilvanhisna Emka Fitri[1, a], Fabrizal Adam Pramudya[2] and Arizal Mujibtamala Nanda Imron[3, b]

[1,2] *Informatics Engineering, Information Technology Department, Jember Polytechnic, Jember, Indonesia*
[3] *Electronics Engineering, Department of Electrical Engineering, Faculty of Engineering, Jember University, Jember, Indonesia*

[a]Corresponding author: zilvanhisnaef@polije.ac.id
[b]arizal.tamala@unej.ac.id

Abstract. Acute respiratory infections (ARI) are infectious diseases that affect both children and adults, particularly in the context of climate change. Bacteria are one of the causes of ARI. According to the government, the discovery of the bacteria that cause ARI is an indicator of successful management of infectious diseases. The current obstacle is the limited number of medical analysts, which results in longer microscopic examination times and requires a high level of objectivity. Therefore, a system for the early detection of ARI-causing bacteria was developed using digital image processing techniques, specifically channel area thresholding as one of the segmentation methods. This research employs four shape features for bacterial classification: the number of bacterial colonies, area, perimeter, and shape. The Naïve Bayes intelligent system method is used for the classification process. The system had an accuracy rate of 86.84% in the classification of four types of bacteria: *S. aureus, S. pneumoniae, C. diphteriae* and *M. tuberculosis.*

ARTICLE INFO

Indonesian Applied Physics Letters

INTRODUCTION

In recent years, global warming has caused climate change, particularly in tropical countries such as Indonesia. Indonesia is experiencing increased rainfall, especially during the rainy season, while it experiences high temperatures and extreme heat during the dry season (Malihah, 2022). Furthermore, air pollution's environmental damage also affects the current climate, which in turn impacts the emergence of acute respiratory infections (ARI) (Herawati et al., 2023). Acute Respiratory Infection (ARI) is a highly contagious disease that affects the upper or lower respiratory tract. It is a major cause of morbidity and mortality worldwide, particularly in children and adults (Indhira and Hendrik, 2023). ARI can be caused by viruses and bacteria, but the focus of this study is on bacteria, including pharyngitis-causing bacteria such as gonorrhea, diphtheria, mycoplasma, and chlamydia, as well as bacteria that cause pneumonia and tuberculosis (Islam, 2023).

Tuberculosis and pneumonia are the two most prevalent infectious diseases in East Java. Jember is one of the districts with the highest number of TB cases, with 5,244 reported cases. Pneumonia is also a leading cause of death among children under five, and its case finding rate in East Java is above 70%. East Java also reported 163 cases. (Dinas Kesehatan Provinsi Jawa Timur, 2023). One effort to control the disease is to detect cases of coughing, sneezing, vomiting, and shortness of breath; patients should seek immediate medical attention and provide sputum or oral specimens for microbiologic examination by a medical analyst (Fitri et al., 2021). However, a limited number of analysts can hinder the early detection of diseases due to longer processing times (Fitri et al., 2022). To develop an early detection system for bacteria that cause ARI, researchers can use computer vision.

Microscopic image analysis is used to identify the presence of Mycobacterium tuberculosis (M. tuberculosis) by using features like area, eccentricity, aspect ratio, compactness, circularity, and roughness (Reshma and Beegum, 2017) and segmentation using Channel Area Thresholding (CAT) (Mithra and Emmanuel, 2018). Additionally, the LVQ accurately detects bacilli that cause acute respiratory infections such as tuberculosis and diphtheria with 97% accuracy (Fitri et al., 2022). Bacteria causing ARI were classified not only by LVQ, but also by KNN method with value K = 3, 5, 7. The best accuracy was 91.7% (Fitri et al., 2021). This research aims to develop a system by comparing it to other methods, such as Naive Bayes, due to its simplicity and high accuracy (Mahran et al., 2020).

RESEARCH METHODOLOGY

The research is divided into six stages (a) : literature study, creation of bacterial image datasets, system design and development, system testing and analysis. The system design and development stage is further divided into four stages (b): data preprocessing, segmentation, feature extraction, and bacterial classification, as shown in Figure 1.

| (a) | (b) |
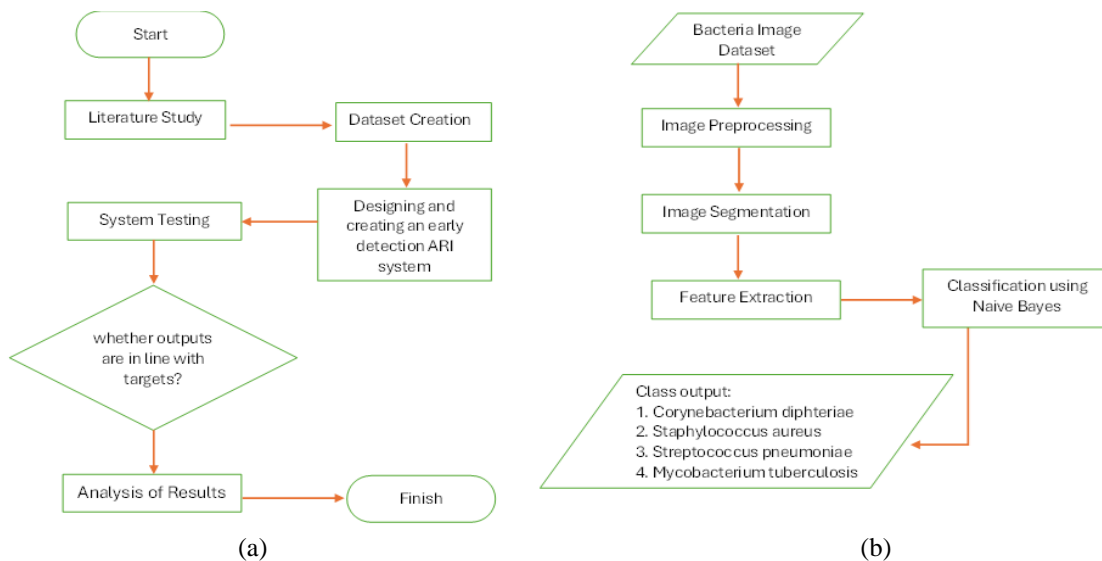
FIGURE 1. (a) The research phase and (b) the system development phase.

Indonesian Applied Physics Letters

Generally, bacteria have three forms, namely cocci, bacilli and sprochetes (Mahon and Lehman, 2019), In this study, bacteria were analyzed, including chain-shaped cocci bacteria (streptococci), grape-like clustered bacteria (staphylococci), and bacillus bacteria such as club-shaped pleomorphic rods and aerobic acid-fast rods obtained from the Balai Besar Laboratorium Kesehatan (BBLK) Surabaya (Figure 2) (Fitri et al., 2021). This study analyzed bacterial preparations by Gram and Ziehl-Neelson (ZN) staining.

1. Gram-positive cocci in graplike cluster (Staphylococci)
2. Gram-positive cocci in chains (Steptrococci)
3. Gram-positive cocci with capsules (Pneumococci)
4. Gram-positive, clubshaped, pleomorphic rods (Corynebacteria)
7. Gram-negative diplococci, adjacent sides flattened (neisseria)
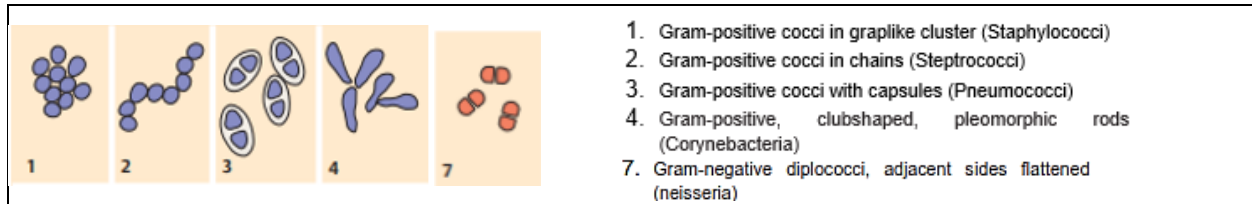
FIGURE 2. Bacterial morphology (Kayser, 2005)

Dataset Creation

The bacterial preparation image is 1920x1080 pixels, then cropped to 151x151 pixels to reduce computational load and eliminate unnecessary background, as shown in Figure 3. The cropping process is based on the shape of the bacteria as shown in Figure 2. A total of 378 images were used, including 94 images of *Corynebacterium diphteriae*, 90 images of *Staphylococcus aureus*, 107 images of *Streptococcus pneumoniae*, and 87 images of *Mycobacterium tuberculosis*.

(a)
(b)
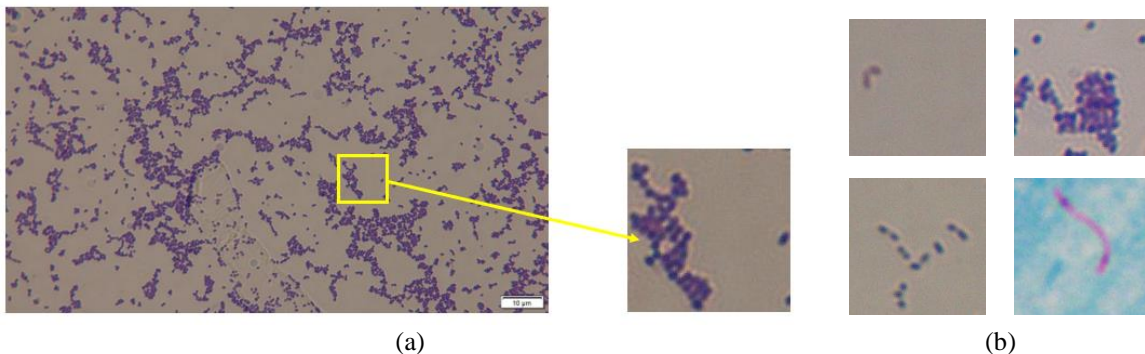
FIGURE 3. (a) ARI bacteria cropping process and (b) 4 bacteria image dataset.

Designing and Creating System

There are two main stages in this phase: designing the system and building the system. The system design includes three menus: home, description, and image processing (see Figure 4). It consists of four steps: data pre-processing, segmenting, feature extraction, and bacterial classification.

(a) homepage

(b) description page

Indonesian Applied Physics Letters
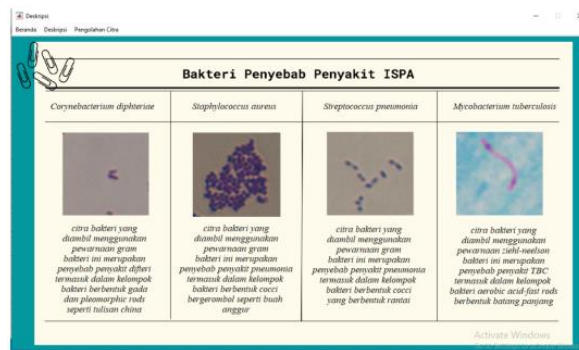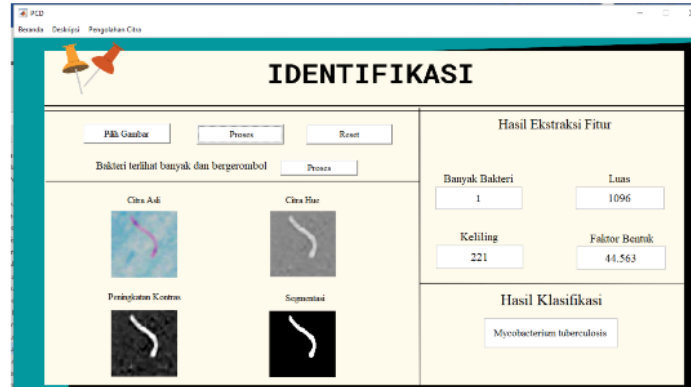
(c) image processing page

FIGURE 4. Display of some app menus

Image Preprocessing

Cropping and converting the image to HSV color space is the first step of preprocessing. This is because the RGB image has a high value, which makes segmenting difficult (Fitri and Imron, 2021). The HSV color space uses a model similar to human vision, specifically cone cells, using the formula equation:

$$hue = tan\left(\frac{3x(G-B)}{(R-G)+(R-B)}\right)$$
$$saturation = 1 - \frac{min(R,G,B)}{V}$$
$$Value = \frac{R+G+B}{3}$$

Furthermore, the image should also increase contrast to achieve a higher contrast value. Increasing contrast affects the histogram graph, which is stretched after determining the minimum and maximum values as limits (Erwin and Ningsih, 2020) using the formula equation:

$$Contrast\,(x,y) = \frac{f(x,y) - min}{\max - min}x1$$

Contrast (x,y) represents the output image after contrast stretching, while f(x,y) represents the input image.

Image Segmentation

Aim of this stage is to use threshold value to separate object from background and obtain a binary image. We use the equation based on the gray value of the image histogram to determine the threshold (T).

$$Segmentation\,(x,y) = \begin{cases} 1, if\ T_1 \le S(x,y) \le T_2 \\ 0, if\ S(x,y) < T_1 \\ 0, if\ S(x,y) > T_2 \end{cases}$$

In addition to the thresholding segmentation process to obtain the shape of the bacteria as shown in Figure 2, the segmentation process is performed based on the area threshold, known as channel area thresholding. (Destarianto et al., 2022).

$$Area_{New} = T_{area1} \le Area_{old} \le T_{area2}$$

Indonesian Applied Physics Letters

Feature Extraction

(Fitri et al., 2021) said that to classify 4 types of bacterial images that cause ARI using 4 shape features, namely the number of bacterial colonies, area, perimeter and shape obtained using the formula equation :

$$Area = Number\ of\ pixels\ in\ row - 1 + row\ to - 2 + \cdots + row\ to - 8$$
$$Perimeter = \sum Even\ code + \sqrt{2}\,x \sum odd\ code$$
$$Shape = \frac{Perimeter^2}{Area}$$

Classification using Naïve Bayes

This research uses the Naive Bayes algorithm, which is based on probabilities and has the advantage of requiring only a small amount of data while maintaining high accuracy (Asmara et al., 2018). The Naïve Bayes algorithm begins with the following steps:

1. Calculate the prior probability of each existing class.
2. Calculate the mean value of each feature using the formula equation :

$$\mu = \frac{\sum n}{k}$$

   Where k = number of data and n = data value

3. Calculate the standard deviation (sd) value of the feature using the formula equation:

$$Sd = \sqrt{\frac{n\sum_{i=1}^{n}(xi - \bar{x})^2}{(n-1)}}$$

4. Calculate the probability density using the equation :

$$g(x,\mu,\sigma) = \frac{1}{\sqrt{2\pi\sigma^2}} e^{-\frac{(x-\mu)^2}{2\sigma^2}}$$

5. Calculate the probability of each class using the provided formula after obtaining the probability density and prior values:

$$P = P(X|Ci)\ x\ P(Ci)$$

RESULT AND DISCUSSION

The research begins by converting the RGB color space to the HSV color space, which allows the bacteria to appear in the Hue, Saturation, and Value channels, as shown in Figure 5. The RGB color space is difficult to segment because of its wide 24bit color range, so you need to decompose into RGB components or convert to another color space. HSVs are chosen because their cone model is like that of human eye cone cells, making it an appropriate choice for representing bacterial shape.
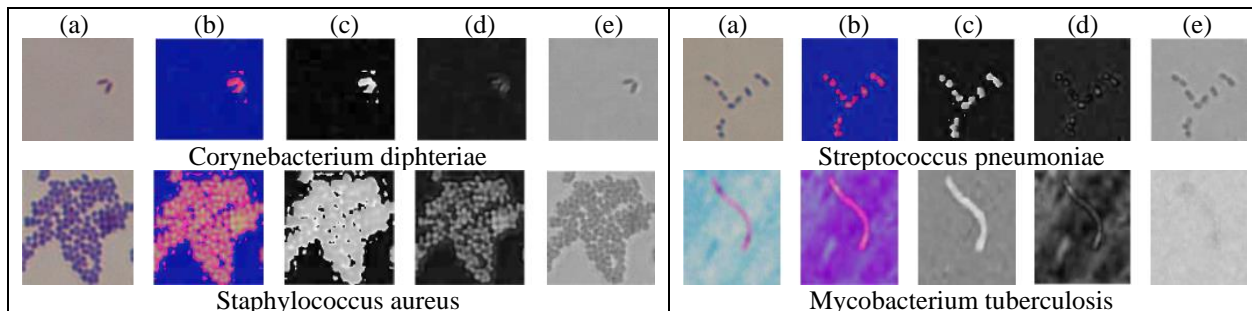
FIGURE 5. (a) Original image, (b) HSV image, (c) Hue image, (d) Saturation image and (e) Value image

Based on the results shown in Figure 5, the hue channel images provide the best representation of the shape of the four bacterial species and are used as the input for the enhancement operation. The main goal of this process is to improve the clarity of the shape of the bacteria, especially that of the M. tuberculosis bacteria. Importantly, this process also affects the histogram, resulting in an even distribution of gray values across all intensity scales, as shown in Figure 6.

(a)   (b)
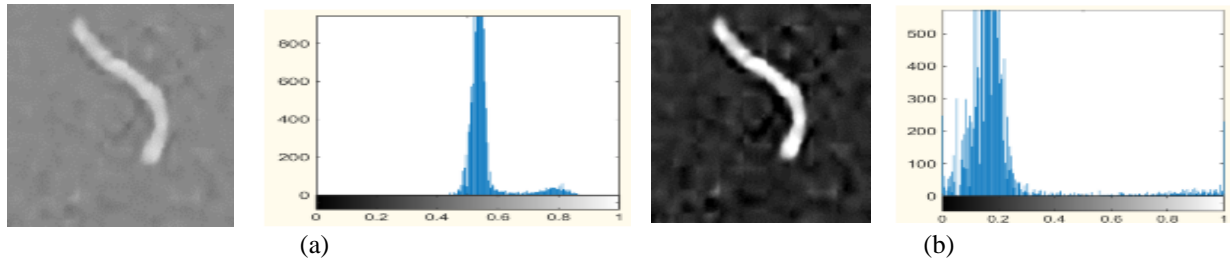
FIGURE 6. (a) Original image and its histogram, and (b) Contrast stretching image and its histogram

Fitri et al. (2021) stated that the segmentation process requires two threshold values: $T_1 = 0.4$ and $T_2 = 0.7$. The segmentation process produces a binary image with two values: 1 (white) and 0 (black) (see Figure 7a). The resulting image may contain noise, such as small spots (from Gram's stain or ZN) and bacterial colonies, which can lead to ambiguity in the identification of clustered forms of bacteria, such as *S. pneumoniae* and *S. aureus*. Therefore, this method uses segmentation based on area, also known as Channel Area Thresholding (CAT). Two thresholds are used, but each bacterium is given a different treatment, as in previous studies. Figure 7 shows that $T_{area1} = 70$ and $T_{area2} = 5000$ were used for three bacteria, S. pneumoniae, C. diphtheriae and M. tuberculosis, whereas $T_{area1} = 80$ and $T_{area2} = 8000$ were used for S. aureus.

(a)

(b)
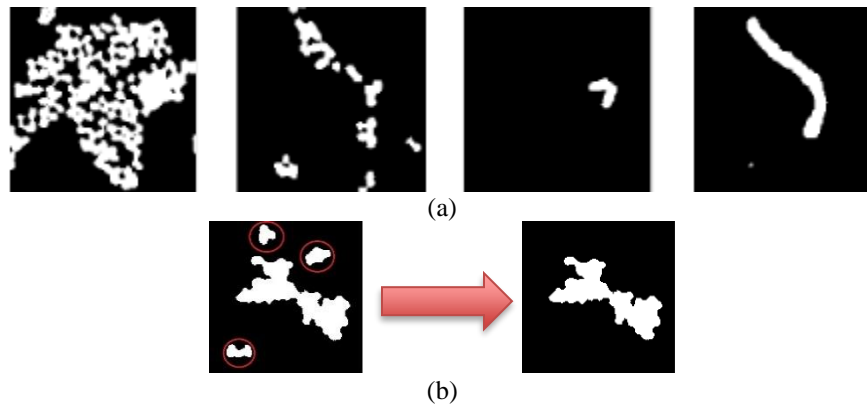
FIGURE 7. Segmentation is performed using two methods, (a) thresholding and (b) channel area thresholding (CAT).

The next step in the segmentation process is feature extraction, which involves the identification of the most prominent and distinguishing features among the four bacteria, such as the number of colonies, the area, the perimeter, and the shape (see Table 1). The minimum, maximum, and mean values for each feature are used as input values for the Naïve Bayes algorithm. The table shows that the largest number of colonies for S. aureus bacteria is 25, while for S. pneumoniae it is 17. However, the largest area for S. aureus is 6166 pixels, while for *S. pneumoniae* it is 3078 pixels. The perimeter and shape feature values are largest for S. aureus and smallest for *M. tuberculosis* bacteria.

Indonesian Applied Physics Letters

TABLE 1. Morphological feature values of each bacterium

Features		C. diphteriae	S. aureus	S. pneumoniae	M. tuberculosis
Colony Number	Min	1	4	2	1
	Max	6	25	17	2
	Mean	2	13	8	1
Area	Min	175	851	331	447
	Max	1136	6166	3078	1545
	Mean	386	2615	629	868
Perimeter	Min	50	313	127	89
	Max	293	1978	741	297
	Mean	119	948	302	166
Shape	Min	12,30	115,12	47,86	17,72
	Max	109,58	787,06	308,50	61,37
	Mean	38,27	355,21	146,12	32,56

The probability value for each class must be calculated, followed by the mean (see Table 1) and standard deviation value of each class (see Table 2), according to the steps of the Naive Bayes algorithm. Classification is performed by comparing training and test data with different percentages of the total data of 378 images, as described in Table 3.

TABLE 2. Morphological characteristic values for each bacterium

The bacteria	P(Ci| bacteria)	Standar deviasi			
		Colony Counts	Area	Perimeter	Shape
C. diphteriae	0,249	1,14	200,77	56,62	21,95
S. aureus	0,24	4,88	975,60	306,89	128,59
S. pneumoniae	0,284	2,92	414,58	106,85	53,82
M. tuberculosis	0,228	0,16	250,43	41,54	10,65

TABLE 3. The results of accuracy, precision and recall of the system on each comparison of training data and test data.

Comparison of training data and testing data	Accuracy (%)	Precision	Recall
50 : 50	86,77	0,875	0,868
60 : 40	86,76	0,876	0,868
70 : 30	84,96	0.857	0,850
80 : 20	86,84	0,891	0,868
90 : 10	86,84	0,884	0,868

Table 3 shows that the Naïve Bayes method produces the highest system accuracy of 86.84% in a data comparison of either 80:20 or 90:10. However, there is a difference in the precision values between the two comparisons. The system precision for the 80:20 comparison is 0.891, while for 90:10 it is 0.868. The precision value indicates the proportion of correctly classified positive category data out of the total positive classified data, while recall indicates the percentage of positive category data that is correctly classified by the system. Based on these results, the optimal data comparison for classifying the four bacterial cells that cause ARI is 80% training data and 20% test data from 378 bacterial image data.

One example of the calculation of testing a random unclassified data, known features number of colonies = 1, area = 1096, perimeter = 221 and shape = 44.56 then to classify the data must be calculated probability density and probability of each class as shown in Table 4. The data are classified by determining the maximum probability value between classes. Based on the table, the maximum value is 0.0000059771718, so the random data is classified into the *M. tuberculosis* class.

Indonesian Applied Physics Letters

TABLE 4. Calculation of probability density and inter-class probability.

The bacteria	Probability Density				Probability (P)
	Colony Counts	Area	Perimeter	Shape	P = P(X|Ci) x P(Ci)
C. diphteriae	0,227	0,0001	0,0120	0,0826	0,0000000054186
S. aureus	0,0105	0,0041	0,0016	0,0023	0,0000000000391
S. pneumoniae	0,0121	0,0135	0,0256	0,0096	0,0000000114034
M. tuberculosis	0,9876	0,0159	0,0251	0,0666	0,0000059771718

Comparison with the previously used K-Nearest Neighbor method is the next step. However, in this study we compared with the 80:20 with the value of K=3, 5, 7 as shown in Table 5.

TABLE 5. K-Nearest Neighbor accuracy, precision and recall results.

	Comparison of the data 80 : 20			
	K = 3	K = 5	K = 7	K = 9
Accuracy (%)	93,42	92,11	92,11	92,11
Precision	0,934	0,921	0,921	0,921
Recall	0,934	0,921	0,921	0,921

As shown in Table 5, the KNN method has the highest accuracy rate, 93.42 %, when comparing 80:20 data, which indicates that the KNN method is better than the Naive Bayesian method, which has the highest accuracy rate, 86.84 %. KNN methods classify data based on Euclidean distance, and then assign priority classes to K-values, while Bayesian methods classify data based on probability values between classes. Compared to previous research, using Channel Area Thresholding in the segmentation process improves the shape of bacterial cells, thus increasing the accuracy of the system.

CONCLUSION

This research aims to apply the Channel Area Thresholding method as one of the segmentation processes for early detection of bacteria causing Acute Respiratory Infection (ARI). This method uses the Naive Bayes algorithm to classify bacteria. The method could classify four bacteria causing ARI with an accuracy rate of 86.84%. When compared with the K-NN method, the best accuracy rate was 93.42%.

REFERENCE

1. R.A. Asmara, B.S. Andjani, U.D. Rosiani, and P. Choirina, "Klasifikasi Jenis Kelamin Pada Citra Wajah Menggunakan Metode Naive Bayes," *Jurnal Informatika Polinema* 4: 3 (2018) 212.
2. P. Destarianto, A.N. Noviana, Z.E. Fitri, and A.M.N. Imron, "Detection of Essential Thrombocythemia based on Platelet Count using Channel Area Thresholding," *Jurnal RESTI (Rekayasa Sistem dan Teknologi Informasi)* 6: 1 (2022) 9–15.
3. Dinas Kesehatan Provinsi Jawa Timur, *Profil Kesehatan Provinsi Jawa Timur Tahun 2022* (Surabaya: Dinas Kesehatan Provinsi Jawa Timur, 2023) <https://dinkes.jatimprov.go.id/userfile/dokumen/PROFIL KESEHATAN JATIM 202022.pdf> Accessed.
4. Erwin and D.R. Ningsih, "Improving Retinal Image Quality Using the Contrast Stretching, Histogram Equalization, and CLAHE Methods with Median Filters," *International Journal of Image, Graphics and Signal Processing* 12: 2 (2020) 30–41.
5. Z.E. Fitri and A.M.N. Imron, "Classification of White Blood Cell Abnormalities for Early Detection of Myeloproliferative Neoplasms Syndrome Using Backpropagation," in Triwiyanto, H.A. Nugroho, A. Rizal, and W. Caesarendra, eds., *Proceedings of the 1st International Conference on Electronics, Biomedical Engineering, and Health Informatics* ,Lecture Notes in Electrical Engineering (Singapore: Springer Singapore, 2021).
6. Z.E. Fitri, L.N. Sahenda, P.S.D. Puspitasari, P. Destarianto, D.L. Rukmi, and A.M.N. Imron, "The The Classification of Acute Respiratory Infection (ARI) Bacteria Based on K-Nearest Neighbor," *Lontar Komputer : Jurnal Ilmiah Teknologi Informasi* 12: 2 (2021) 91.
7. Z.E. Fitri, L.N. Sahenda, P.S.D. Puspitasari, and A.M.N. Imron, "Identification of Bacilli Bacteria in Acute Respiratory Infection (ARI) using Learning Vector Quantization:," in presented at the *2nd International Conference on Social Science, Humanity and Public Health (ICOSHIP 2021)* (Jember, Indonesia: 2022).

8. A.T. Herawati, S.W. Megawati, V.J. Anggraeni, S. Kartadarma, A. Kandanisa, and N.L.B. Astuti, "Optimalisasi Peran Ibu dalam pencegahan ISPA (Infeksi Saluran Pernafasan Akut) Anggota Keluarga di Musim Hujan," *Jurnal Abdimas (Journal of Community Service): Sasambo* 5: 2 (2023) 368–373.

9. S. Indhira and B. Hendrik, "Penerapan Data Mining Menggunakan Algoritma K-Means Untuk Klasifikasi Penyakit ISPA," *Journal of Information System and Education Development (JISED)* 1: 3 (2023) 31–35.

10. S. ul Islam, *Infectious diseases smart study guide for medical students, residents, and clinical providers* (Amsterdam: Academic Press, 2023).

11. F.H. Kayser, ed., *Medical microbiology* ,Thieme Flexibook (Stuttgart New York: Thieme, 2005).

12. C.R. Mahon and D.C. Lehman, eds., *Textbook of diagnostic microbiology* (Sixth edition) (St. Louis, Missouri: Elsevier Saunders, 2019).

13. A.A. Mahran, R.K. Hapsari, and H. Nugroho, "Penerapan Naive Bayes Gaussian Pada Klasifikasi Jenis Jamur Berdasarkan Ciri Statistik Orde Pertama," *Network Engineering Research Operation* 5: 2 (2020) 91.

14. L. Malihah, "Tantangan Dalam Upaya Mengatasi Dampak Perubahan Iklim Dan Mendukung Pembangunan Ekonomi Berkelanjutan: Sebuah Tinjauan," *Jurnal Kebijakan Pembangunan* 17: 2 (2022) 219–232.

15. K.S. Mithra and W.R.S. Emmanuel, "Segmentation of Mycobacterium Tuberculosis Bacterium From ZN Stained Microscopic Sputum Images," in *2018 International Conference on Smart Systems and Inventive Technology (ICSSIT)* presented at the *2018 International Conference on Smart Systems and Inventive Technology (ICSSIT)* (Tirunelveli, India: IEEE, 2018).

16. S.R. Reshma and T.R. Beegum, "Microscope image processing for TB diagnosis using shape features and ellipse fitting," in *2017 IEEE International Conference on Signal Processing, Informatics, Communication and Energy Systems (SPICES)* presented at the *2017 IEEE International Conference on Signal Processing, Informatics, Communication and Energy Systems (SPICES)* (Kollam: IEEE, 2017).

Review of Application YOLOv8 in Medical Imaging

Aisyah Widayani [1, a)], Ayub Manggala Putra [1, b)], Agiel Ridlo Maghriebi [1)], Dea Zalfa Cahyla Adi [1)], Moh. Hilmy Faishal Ridho[1)]

[1] *Radiology Imaging Technology, Department of Health, Faculty of Vocational Studies, Universitas Airlangga, Surabaya, Indonesia.*

[a)] Corresponding author: aisyahwidayani@gmail.com
[b)] ayubmanggala.vokasi@drive.unair.ac.id

Abstract. Deep learning has revolutionized medical imaging analysis, with YOLOv8 emerging as a promising tool for various tasks like lesion detection, organ segmentation and disease classification. This review investigates YOLOv8's applications across diverse medical imaging modalities (X-Ray, CT-Scan and MRI). We conducted a systematic literature search across databases like Pubmed, ScienceDirect and IEEE to identify relevant studies evaluating YOLOv8's performance in medical imaging analysis. YOLOv8 achieved high performance for meningioma and pituitary tumors with and without data augmentation (precision >0.92, recall >0.90, mAP >0.93). Glioma detection showed lower performance but still promising results (precision >0.86, recall >0.81, mAP >0.86). Breast cancer detection with SGD optimizer yielded best performance with an average mAP of 0.87 for mass detection. The model achieved high accuracy in detecting normal (mAP 0.939) and malignant lesions (mAP 0.911). YOLO v8 on Dental radiograph successfully detected cavities, impacted teeth, fillings and implants (precision of >0.82, recall of >0.78 and F1-Score of >0.80). Lastly, for lung disease classification, YOLOv8 achieved high accuracy (99.8% training and 90% validation) in classifying normal, COVID-19, influenza and lung cancer disease. With the importance to improve clinical decision-making and patient outcomes in healthcare, the YOLOv8 algorthm underscores the importance of pre-processing, augmentation and optimization of key hyperparameters.

ARTICLE INFO

INTRODUCTION

Computer vision is an aspect of artificial intelligence that can enable computers to perform various tasks such as seeing, feeling, and making decisions. One important part of computer vision is detecting objects. Object detection works by determining the location and position of the object, as well as the label contained in the bounding box (Mahendru and Dubey, 2021). Object detection applications are widely applied in various fields, one of which is the application in the medical field which is used for medical image processing. In medical image processing, identification and localization are needed to find abnormalities in medical images (Qureshi et al., 2023). The assistance of artificial intelligence and deep learning provides opportunities to increase precision and effectiveness in diagnosing various abnormalities in medical imaging.

The deep learning algorithm that is frequently used to detect objects is YOLOv8 (You Only Look Once version 8), with the ability to provide high precision and real-time detection (Palanivel et al., 2023). YOLO is included in the one-stage-detector category, which means it only requires one pass through a neural network and predicts all objects accompanied by bounding boxes (Shetty et al., 2021). The YOLOv8 algorithm is an improved version of the YOLOv3 algorithm, with a wider backbone implementation supported by feature fusion techniques to increase accuracy in detecting objects (Osama, Kumar and Shahid, 2023). The following is the architecture of YOLOv8 in Figure 1.
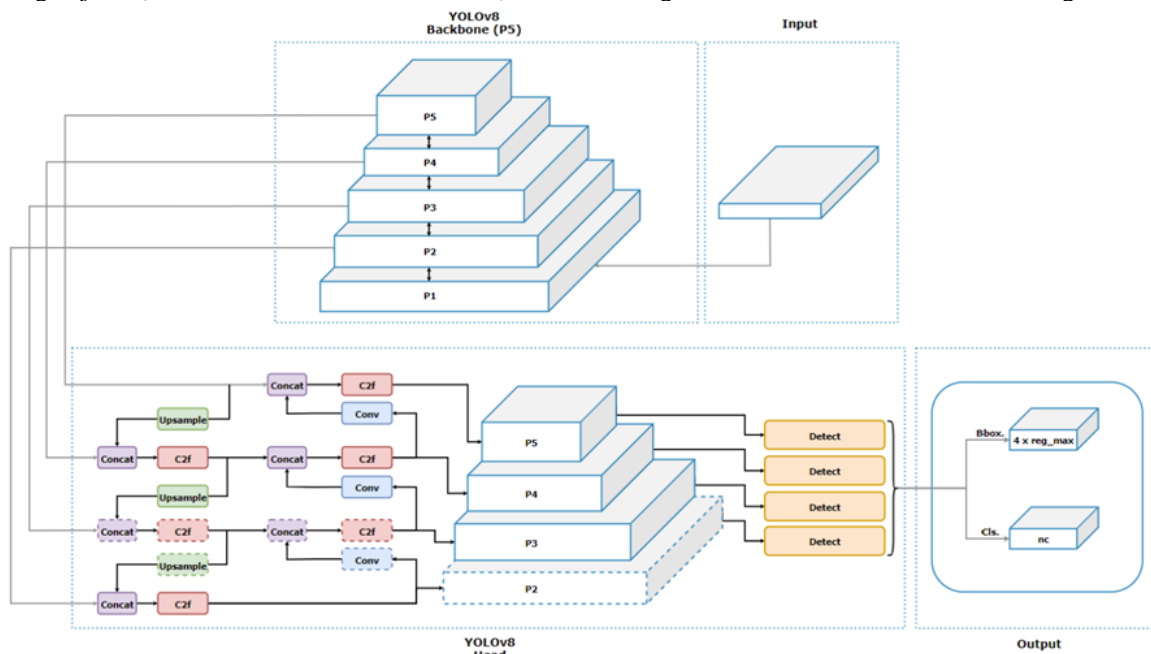
FIGURE 1. YOLOv8 Architecture (Karna *et al.*, 2023)

The YOLOv8 architecture consists of several parts, including CSPDarknet53 Feature Extractor, C2F Module, Detection Head, and YOLOv8-Seg Model (Khare et al., 2023). Each part of YOLOv8 will be discussed one by one.

1. **CSPDarknet53 Feature Extractor** is used as a feature extractor, which consists of convolution layers, batch normalization, and SiLU activation function. Feature extraction was improved in YOLOv8 by changing the convolution layers to 3x3 from the previous 6x6.

2. **C2F Module** implemented in YOLOv8 combines high-level features with contextual information. The combined output of a bottleneck block consists of two 3x3 convolutions with residual connections. The goal is to improve feature representation.

3. **Detection Head** consists of several components, including:

Indonesian Applied Physics Letters

a. **Independent Branches** which allows each branch to carry out certain tasks. This affects the overall detection accuracy.
b. **Activation Function** represents the existence of an object within a bounding box, and allows an object to be classified in a class.
c. **Loss Function** is used to optimize the model using CioU (Complete Intersection over Union) and DFL (Dynamic Focal Loss). Its function is to increase the effectiveness of object detection, especially on small objects.

4. **YOLOv8-Seg Model** is a semantic segmentation model in YOLOv8, so it is called YOLOv8-Seg. This enables broad functionality for a variety of computer vision tasks.

Therefore, this study will discuss several studies that apply the YOLOv8 deep learning algorithm for analysis and diagnosis in medical imaging. The review carried out will support researchers and professionals, especially in the health sector, to understand how the YOLOv8 algorithm works, as well as its benefits in medical object detection applications. In the future, it is hoped that deep learning algorithms for detecting objects can be developed for wider medical applications. This research is composed of Research and Methodology which discusses the approach used and combines data obtained from the included research. The next chapter, related to Results and Discussion, examines the stages carried out before implementing the YOLOv8 algorithm, for example pre-processing and augmentation; then the applied detection class; Data sharing for training, testing and validation processes; implemented hyperparameters, such as epoch, batch, image size, etc; to the training chart results for each study. Then, the last chapter is the conclusion.

RESEARCH METHODOLOGY

This chapter outlines the methodological approach employed to investigate the current landscape of YOLOv8 applications in medical imaging. We conducted a systematic literature search to gather and analyze relevant research studies. This approach ensures a comprehensive and unbiased evaluation of the field's current state and future directions.

Searching Strategy

We employed a multi-database approach, querying relevant publications from PubMed, IEEE and Science Direct. Our search strategy utilized a combination of keywords including "YOLOv8," "medical imaging," "object detection," "segmentation," and "classification" connected by Boolean operators (e.g., "AND," "OR"). We narrowed our search parameters to studies published post-2023 in order to encompass the latest developments in this evolving field, taking into account the release of YOLOv8 in January 2023. After retrieving the initial search results, we implemented a screening process based on pre-defined inclusion and exclusion criteria.

Studies were included if they:
1. Focused on the application of YOLOv8 for medical imaging tasks.
2. Utilized peer-reviewed research methodologies and presented the original research results.
3. Utilized medical imaging datasets acquired from human participants.
4. Evaluated the performance of YOLOv8 using established metrics relevant to the specific medical imaging such as accuracy, precision, recall, F1 score.
5. Released in the English language.

To ensure a targeted analysis of primary research on YOLOv8's application in medical imaging, we implemented the following exclusion criteria:
1. Reviews, editorials, or letters.
2. Studies not published in English.
3. Studies not evaluating YOLOv8.
4. Studies lacking peer-reviewed methodology or original findings.
5. Studies not using established metrics to assess YOLOv8 performance.
6. Studies solely focused on animal models.

Through this process, we identified a collection of relevant studies that formed the foundation for our review and analysis of YOLOv8's contributions to the field of medical imaging.

Evidence Synthesis

Following the initial literature search and application of inclusion/exclusion criteria, the retrieved studies underwent critical appraisal. This involved extracting relevant data points, such as the specific medical imaging modality (e.g., X-ray, CT scan, MRI), the addressed medical imaging task (e.g., lesion detection, organ segmentation), and the reported performance metrics (accuracy, precision, recall).

This extracted data then served as the foundation for a qualitative thematic analysis. This analytical approach aimed to identify recurring themes within the studies, including strengths, weaknesses, and potential research gaps.

RESULT AND DISCUSSION

In this section, we will review several studies using the YOLOv8 model in the field of medical imaging. The first thing that will be discussed is a system diagram which will explain the procedures carried out in the research being evaluated, to find out the steps before implementing the YOLOv8 algorithm. Second, the detection class is the output of the system according to the annotation given to the dataset. Next is the number of datasets used and the division into testing and validation data. Fourth, namely, results related to the accuracy, precision, recall, and F1 Score, which are obtained after the training process as a result of computing. Then, a chart of the training results.

Brain Tumor

The paper entitled "YOLOv8 Based on Data Augmentation for MRI Brain Tumor Detection" (Satila Passa, Nurmaini and Rini, 2023) aims to detect meningiomas, gliomas, and pituitary brain tumors. The data collected from two methods, using without Augmentation and without using Augmentation. The following is a system diagram of the experiments carried out, shown in Figure 2.
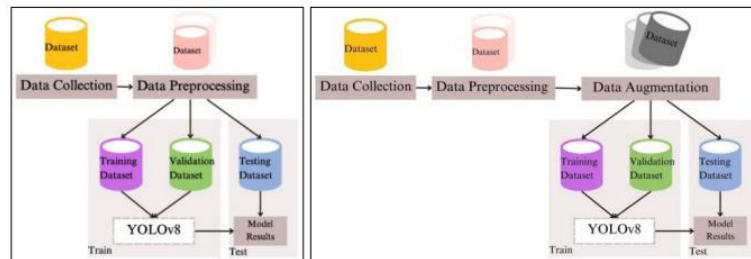
FIGURE 2. (a) Framework without implementing augmentation (b) Implementing augmentation

The first step in this research is collecting data. Data is an important part of creating artificial intelligence (AI) and machine learning (ML). Without relevant and quality data, AI and ML will not be able to produce effective or accurate models. Data taken consist of 3064 T1-weighted contrast-enhanced images with three types of brain tumors such as, meningioma, glioma, and pituitary. The meningioma dataset was separated for training 496, testing 71, and validation 141. Glioma dataset divided into training 998, testing 143, validation 285. Then, 651 training dataset, testing 83, and validation 186 for pituitary.

After getting the required data, the data will be processed. The data processing is to change data from .mat to .jpg format. The next step is data augmentation, which aims to improve the performance of models by training process. There are various techniques applied to this data augmentation such as flip, 90° rotate, crop, rotation, shear, grayscale, brightness, exposure, blur, and noise. Next, training the yolov8 model is performed.

The results of this study evaluate the performance of the YOLOv8 model algorithm for identifying brain tumors, specifically meningioma, glioma, and pituitary tumors. The YOLOv8 hyperparameters used in this research are input

Indonesian Applied Physics Letters

size 640 x 640, 100 epochs, and batch size 8. The results obtained in this research are displayed in two without and with data augmentation. The data obtained without and with data augmentation is shown in Figure 3 and 4. Dataset test result that applied YOLOv8 without augmentation shown in Figure 5, with augmentation in Figure 6.
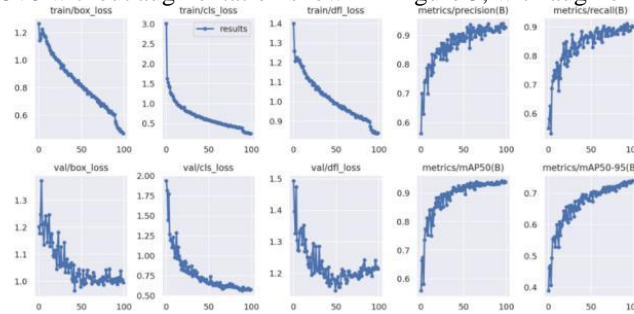

FIGURE 3. Training chart without augmentation
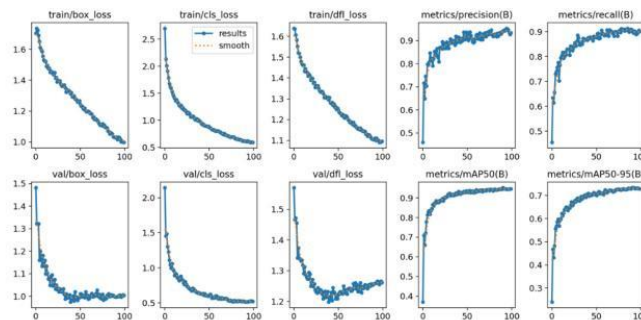
FIGURE 4. Training chart with augmentation

From the data training chart without augmentation (Figure 3), presented for Meningioma tumors, Precision: 0.956, Recall: 0.951, mAP50: 0.98, and mAP50-95: 0.849. Glioma tumors, Precision: 0.866, Recall: 0.816, mAP50: 0.866, and mAP50-95: 0.596. Pituitary tumors, Precision : 0.956, the Recall : 0.939, mAP50 : 0.97, and mAP50-95 : 0.773. Overall performance, Precision : 0.926, Recall : 0.902, mAP50 : 0.938, and mAP50-95 : 0.739.

Figure 4 shows a training chart with augmentation for Meningioma tumors, Precision: 0.985, Recall: 0.95, mAP50: 0.986, and mAP50-95: 0.841. Glioma tumors, Precision: 0.891, Recall: 0.831, mAP50: 0.894, and mAP50-95: 0.599. Pituitary tumors, Precision : 0.95, the Recall : 0.942, mAP50 : 0.975, and mAP50-95 : 0.758. "All" represents overall performance, Precision : 0.942, Recall : 0.908, mAP50 : 0.952, and mAP50-95 : 0.733. Both without and with augmentation, Meningioma dan Pituitary detection get higher precision, recall, and mAP50 scores than Glioma.

FIGURE 5. Result data testing without augmentation

FIGURE 6. Result data testing with augmentation

Breast Cancer

This research (Titisari *et al.*, 2023) focuses on optimizing the YOLOv8s model for breast cancer detection. The input is in the form of a 2D mammography image which is then annotated to indicate the presence of a breast cancer

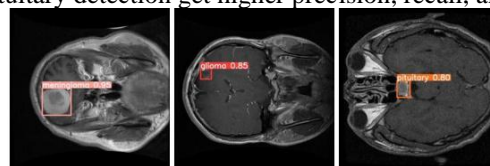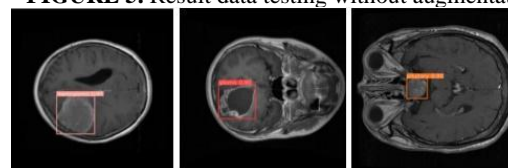mass or lesion. The next pre-processing stage begins with equalizing the image size by reducing the image pixel size to 640x640. Augmentation is carried out to increase the amount of data so that it is more varied. The respective experiment, the system trained applying three optimization methods, i.e. Adam, SGD, and RMSPropagation restrictions and set up different hyperparameters related to epoch 75, batch size 16. Diagram Research Flow shown on Figure 7.
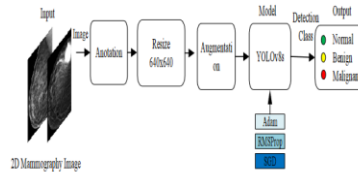

FIGURE 7. Diagram Research Flow of Breast Cancer Detection

The dataset, a mammography image, originating from the Categorized Digital Database for Low Energy and Subtracted Contrast Enhanced Spectral Mammography Images (CDD-CESM), a public dataset. A total of 2,085 mammography images were used after going through a data augmentation process. Of these, there were 809 normal images, 432 benign images, and 844 malignant images. All images are then labeled based on the doctor's medical report on each patient's data. The dataset was then annotated and divided into three subsets, namely 87% as training data, 8% as validation data, and 5% as testing data. In this study, there were a total of 1,824 images used for training, 174 images for testing, and 87 images for evaluation.

The whole work performance of optimizing three different parameters in the YOLOv8s model has been successful in detecting masses or lesions in mammography images. The performance using three optimizers in detecting breast cancer was found that SGD composed **the highest mAP value of 0.87 followed by RMSProp with a value of 0.345 and Adam 0.44.** The SGD optimizer has the fastest training time compared to the other optimizers. Performance of YOLOv8 in detecting normal class, was obtained highest mAP at 0.939 using the SGD optimizer, precision 0.946, and recall of 0.9. The benign class, the highest mAP acquired, utilized the SGD optimizer, precision 0.854, recall 0.667, and mAP 0.762. Whereas, for the Malignant class, the optimum results were also obtained with the SGD optimizer, with a precision of 0.867, recall of 0.871, and mAP of 0.911. Figure 8 shows the confusion matrix of each optimizer.

| (a) | (b) | (c) |
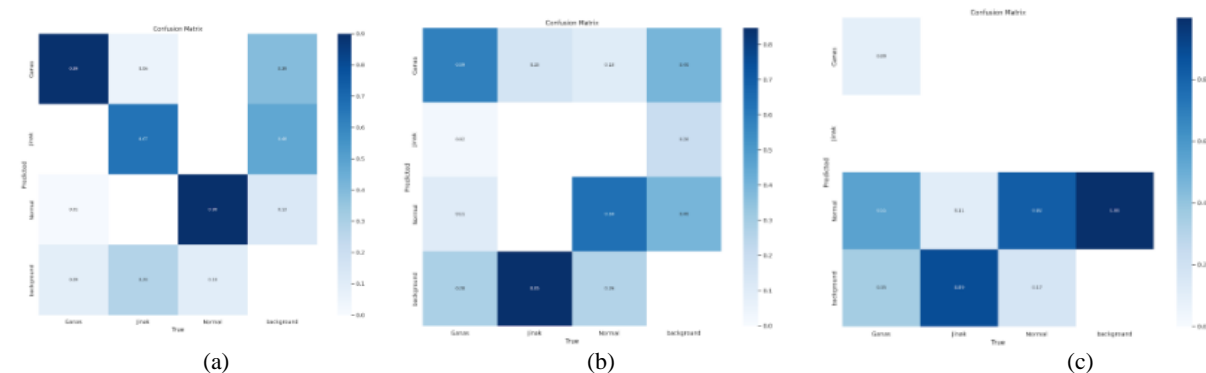
FIGURE 8. Confusion Matrix in a) SGD b) ADAM c) RMSProp
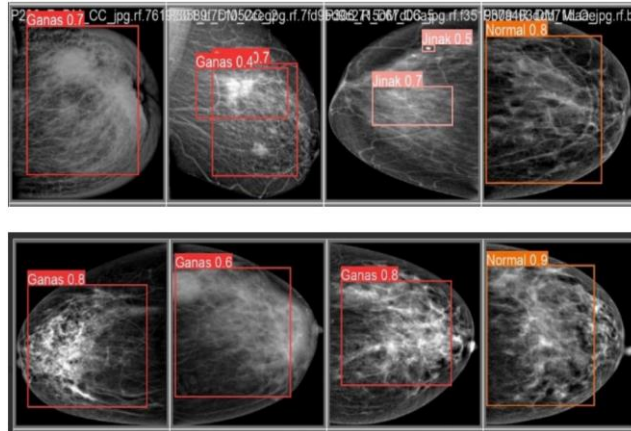
FIGURE 9. Detection Result for Breast Cancer Detection

In Figure 9, There are some classes of detection normal, benign shown as jinak, and malignant displayed as ganas. From the research results, SGD is the best optimizer in detecting masses with an average mAP of 0.87. There was an increase in performance after the tuning process, where accuracy increased from 75% to 85%. The highest mAP value was obtained when detecting the normal (0.939) and malignant (0.911) classes, while when detecting the benign class the value was lower because the amount of benign data was smaller.

Dental Radiography

The application of the YOLOv8 model is also used for analysis and diagnosis in the field of dental radiography. Research (George et al., 2023) states that methods for detecting dental diseases that are carried out manually require time and energy. So, it is important to have an automatic detection system for various dental conditions such as cavities, impacted teeth, fillings and implants on panoramic dental X-rays. The system block diagram from the research carried out is in Figure 10.
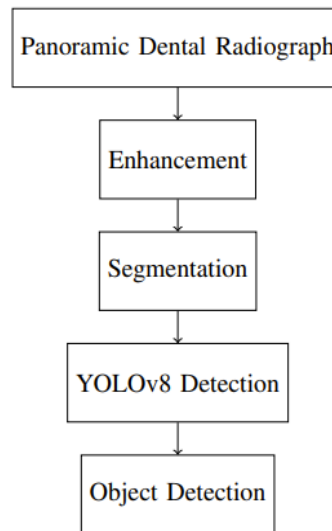
FIGURE 10. Block Diagram of Dental Radiography

Before applying the YOLOv8 model, an enhancement process was carried out to increase the quality of the panoramic dental radiography image by removing noise using a Gaussian Pyramid. In addition, the Laplacian pyramid method is used to increase the detail of the image. Image brightness and contrast are also applied using an automatic algorithm at the enhancement stage.

The segmentation process is carried out to separate four different parts in one image. The segmented parts are divided into extraction of the jaw area, separation of the upper and lower jaw, and vertical segmentation of the upper and lower jaw. The following is an image of an area segmented vertically to separate the upper and lower jaw (Figure .11-14).

FIGURE 11. Top Left Jaw Area

FIGURE 12. Top Right Jaw Area

FIGURE 13. Bottom Left Jaw Area

FIGURE 14. Bottom Right Jaw Area

YOLOv8 is one of the object detection algorithms used to detect the classes determined in this research, namely cavities, impacted teeth, fillings and implants. The number of datasets used is 1269, which are divided into training, testing and validation data, respectively 1015, 63 and 191. There are several hyperparameters used in the training process, namely epoch 35, batch size 16, image size 640, and learning rate 0.001. Precision, recall, and F1-Score are calculated to evaluate the performance of the trained YOLOv8 model. The results obtained for precision were 82.36%, recall 78.38%, and F1 Score 80.32%. The curve results obtained after the training process shown in Figure 15-18, as well as Graphical User Interface (GUI) results which are named "Dental Radiography Analysis and Diagnosis". Users can enter images and the detection process using the YOLOv8 model is shown in Figure 19.
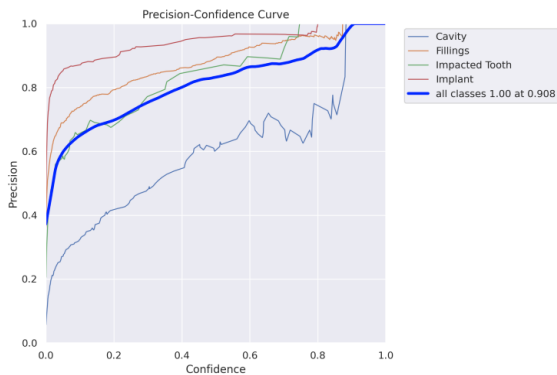
FIGURE 15. Precision-Confidence Curve
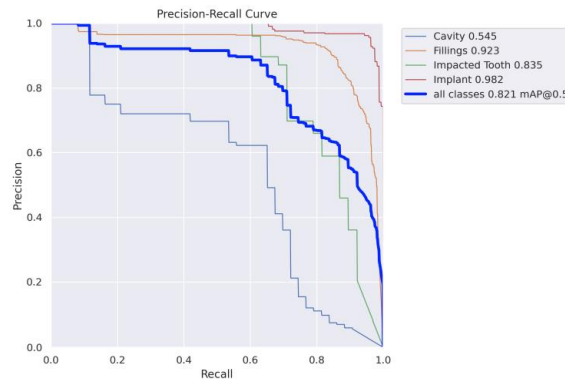
FIGURE 17. Precision-Recall Curve

Indonesian Applied Physics Letters
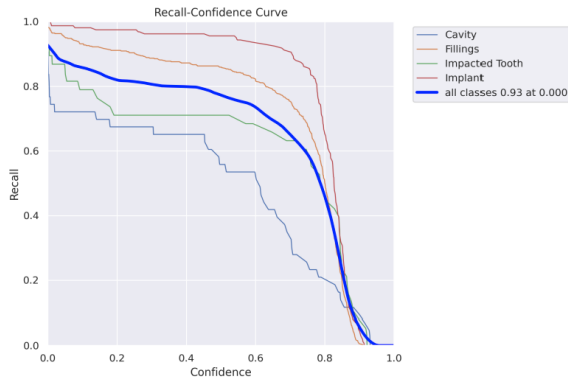
FIGURE 16. Recall-Confidence Curve
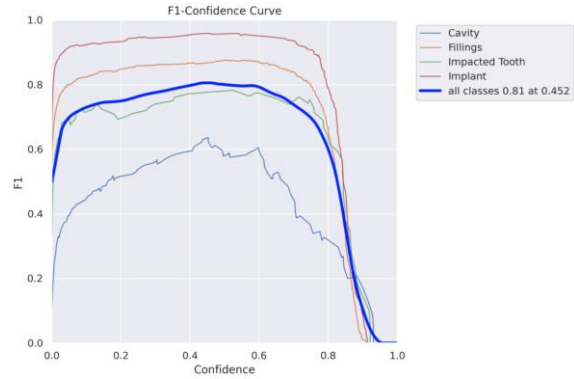
FIGURE 18. F1 Score-Confidence Curve
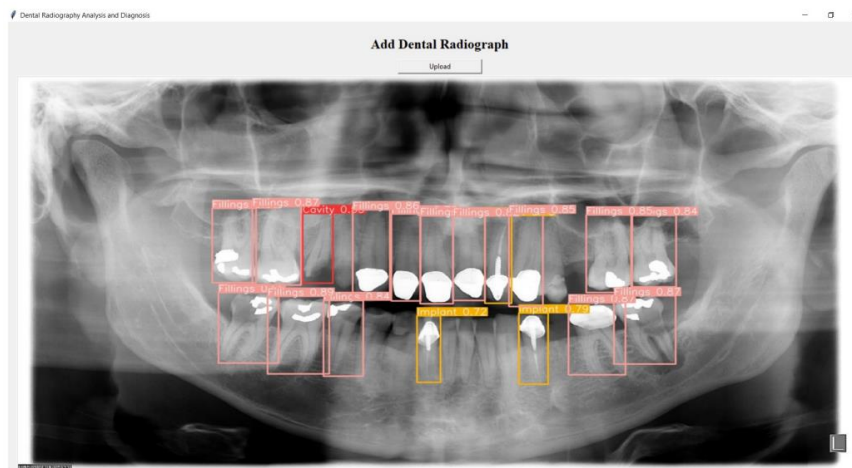
FIGURE 19. GUI of Dental Radiography Analysis and Diagnosis

Lung Disease

In this research, Mousavi *et al.*, 2023 utilized axial lung image results collected from sources such as Kaggle, GitHub, and Radiopedia to import data. The data obtained includes 155 cases of normal, 309 cases of COVID-19, 42 cases of influenza, and 73 cases of cancer. Then, some pre-processing applied to achieve appropriate image quality to avoid ambiguity in detection results. Pre-processing stages are shown in Figure 20.
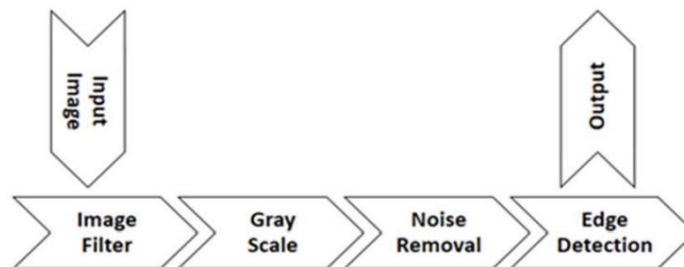
FIGURE 20. Pre-processing stage in Lung Disease Detection

Indonesian Applied Physics Letters

Before the training process, the dataset splits into training, testing, and validation. Normal cases used 100 data train, 50 data testing, and 5 data validation. COVID-19 cases divide to 200 data train, 100 data test, and 9 data validation. Then, Influenza cases separate into 30 data train, 10 data tes, and 2 data validation. Cancer cases distribute data into 50 data train, 20 data tes, and 3 data validation.

There are four types of metrics used to examine the proposed network.i.e. accuracy, precision, recall, and F1-Score. The evaluation metrics included true positives (TP), true negatives (TN), false positives (FP), and false negatives (FN) to assess the proposed network. Where, TP represents the number of true positive predictions, while TN denotes the number of true negative predictions. Additionally, FN indicates the number of false negative predictions, and FP indicates the number of false positive predictions. There are such formulas to present accuracy, precision, recall, and F1-Score. That is shown in Equation below.

$$a = \frac{T_P + T_N}{T_P + T_N + F_P + F_N}$$

$$p = \frac{T_P}{T_P + F_P}$$

$$r = \frac{T_P}{T_P + F_N}$$

$$F_{1-Score} = \frac{2 \times precission \times Recall}{precission + Recall}$$

To determine the accuracy of this study, the researchers used 40 epochs in training. The training accuracy reaches 99.8%, while the validation accuracy achieves 90%. This shows that training provides a very accurate model. Increasing the number of epochs means that it increases the accuracy of the model as well. Loss values recognized are 27% for training, and 0.05% for validation.

FIGURE 21. Confusion Matrix of Lung Disease Detection
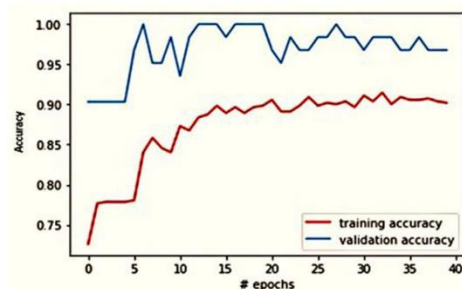
FIGURE 22. The accuracy chart of training models
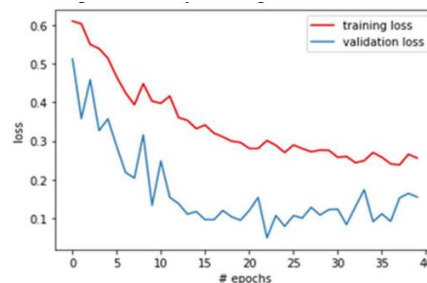
FIGURE 23. The loss chart of training models

Indonesian Applied Physics Letters

CONCLUSION

You Only Look Once version 8 (YOLOv8) algorithm as an object detection model in medical imaging has been applied to detect brain tumors, breast cancer, dental radiography, and lung diseases. Pre-processing has an important role in preparing images with good quality, ensuring that the YOLOv8 algorithm provides accurate information when detecting abnormalities or distinguishing normal conditions. Therefore, this stage is applied in the selected studies. The augmentation process is also significant, aiming to enhance the performance of the YOLOv8 model throughout the training process. The studies discussed herein also delve into hyperparameters, such as epoch, batch size, and image size. Performance metrics including accuracy, precision, recall, and F1-Score are reported to describe the performance results of the YOLOv8 detector, as displayed in the training chart. YOLOv8 demonstrates an important role in enhancing efficiency and accuracy in medical imaging, suggesting its potential to support healthcare in the future. However, continuous research and development are necessary to achieve optimal improvements in healthcare.

REFERENCES

1. George, J. *et al.* (2023) 'Dental Radiography Analysis and Diagnosis using YOLOv8', *9th International Conference on Smart Computing and Communications: Intelligent Technologies and Applications, ICSCC 2023*, pp. 102–107. doi: 10.1109/ICSCC59169.2023.10335023.
2. Karna, N. B. A. *et al.* (2023) 'Toward Accurate Fused Deposition Modeling 3D Printer Fault Detection Using Improved YOLOv8 With Hyperparameter Optimization', *IEEE Access*, 11, pp. 74251–74262. doi: 10.1109/ACCESS.2023.3293056.
3. Khare, O. *et al.* (2023) 'YOLOv8-Based Visual Detection of Road Hazards: Potholes, Sewer Covers, and Manholes', *2023 IEEE Pune Section International Conference, PuneCon 2023*. doi: 10.1109/PuneCon58714.2023.10449999.
4. Mahendru, M. and Dubey, S. K. (2021) 'Real time object detection with audio feedback using Yolo vs. Yolo_V3', *Proceedings of the Confluence 2021: 11th International Conference on Cloud Computing, Data Science and Engineering*, pp. 734–740. doi: 10.1109/Confluence51648.2021.9377064.
5. Mousavi, M. *et al.* (2023) 'YOLO for Lung Disease Detection from CT Scans', *SISY 2023 - IEEE 21st International Symposium on Intelligent Systems and Informatics, Proceedings*, pp. 495–500. doi: 10.1109/SISY60376.2023.10417904.
6. Osama, M., Kumar, R. and Shahid, M. (2023) 'Empowering Cardiologists with Deep Learning YOLOv8 Model for Accurate Coronary Artery Stenosis Detection in Angiography Images', *2023 International Conference on IoT, Communication and Automation Technology, ICICAT 2023*, pp. 1–6. doi: 10.1109/ICICAT57735.2023.10263760.
7. Palanivel, N. *et al.* (2023) 'The Art of YOLOv8 Algorithm in Cancer Diagnosis using Medical Imaging', *2023 International Conference on System, Computation, Automation and Networking, ICSCAN 2023*, pp. 1–6. doi: 10.1109/ICSCAN58655.2023.10395046.
8. Qureshi, R. *et al.* (2023) 'A Comprehensive Systematic Review of YOLO for Medical Object Detection (2018 to 2023)', *Authorea Preprints*, 11. Available at: https://www.authorea.com/doi/full/10.36227/techrxiv.23681679.v1?commit=dba07752d065dca931b3a478 425ead886b201cf2.
9. Satila Passa, R., Nurmaini, S. and Rini, D. P. (2023) 'YOLOv8 Based on Data Augmentation for MRI Brain Tumor Detection', *Scientific Journal of Informatics*, 10(3), p. 363. doi: 10.15294/sji.v10i3.45361.
10. Shetty, A. K. *et al.* (2021) 'A Review: Object Detection Models', *2021 6th International Conference for Convergence in Technology, I2CT 2021*, pp. 1–8. doi: 10.1109/I2CT51068.2021.9417895.
11. Titisari, D. *et al.* (2023) 'Enhancing Breast Cancer Detection: Optimizing YOLOv8's Performance Through Hyperparameter Tuning', *ICITDA 2023 - Proceedings of the 2023 8th International Conference on Information Technology and Digital Applications*, pp. 1–6. doi: 10.1109/ICITDA60835.2023.10427255.

Detection of Throat Disorders Based on Thermal Image Using Digital Image Processing Methods

Franky Chandra Satria Arisgraha[1, a] , Riries Rulaningtyas[1], Endah Purwanti[1], and Fadli Ama[1]

[1]Biomedical Engineering, Department of Physics, Faculty of Science and Technology, Universitas Airlangga

[a]Corresponding author: franky-c-s-a@fst.unair.ac.id

Abstract. Throat disorders are often considered trivial for some people, but if they are not treated immediately, they can result in more severe conditions and require a longer time to cure this disorder. Objective, safe and comfortable detection of throat disorders is important because throat disorders are an indication of inflammation which, if not treated immediately, can have negative consequences. This research aims to detect throat disorders based on thermal images using digital image processing methods. Image capture was carried out with the same color pallete range on the camera, namely 33°C-38°C. The image obtained is then cropped in the ROI, then the image is threshold with a gray degree of 190. Pixels that have a gray degree above 190 are converted to white, while those below the threshold are converted to black. Next, the percentage of each white and black area is calculated compared to the total ROI area. If the percentage of white area is greater than 38% compared to the area of the throat then it is identified as having a throat disorder, whereas if the percentage of white is less than 38% then it is identified as not having a throat disorder. The detection program created provides an accuracy of 87.5% on sample data of 8 test data.

ARTICLE INFO

INTRODUCTION

Throat disorders are often considered trivial for some people, but if they are not treated immediately they can result in more severe conditions and require a longer time to cure this disorder. Objective, safe and comfortable detection of throat disorders is important because throat disorders are an indication of inflammation which, if not treated immediately, can have negative consequences. Inflammation of the throat can cause the temperature around the site of inflammation to become higher. One of the efforts made to detect body temperature non-invasively is using a thermo gun. However, thermo gun can only be used to measure body temperature in a relatively narrow area and need to be done at a very close distance, namely less than one centimeter. It is important to identify symptoms of the disorder as early as possible to prevent the condition from getting worse (Cristina, 2020). Thermal Camera is a tool to determine the temperature distribution of an object by using FPA (focal plane array) technology as a detector that will receive infrared signals. Thermal cameras are able to record objects in image form, so that all areas of the object that can be recorded by the camera can have their temperature measured at the same time, temperature variations emitted from the object are then converted into images that can be interpreted by experts. Thermal Cameras have been used for various purposes, including in medical diagnostics or clinical trials. The use of thermal cameras in the medical field includes detection breast cancer, determining wound status, and diagnosing deep vein thrombosis as well as diagnosing various other diseases (Seydi, 2017). In carrying out the correct interpretation of images, a quantitative approach is needed which can be obtained through digital image processing (Sumriddetchkajorn, 2016). The problem to be solved in this research is how to detect throat disorders safely and objectively and to find out the performance of methods for detecting throat disorders. The aim of this research is to detect throat disorders based on thermal images using digital image processing methods and to determine the performance of detecting throat disorders based on thermal images using digital image processing methods. This research is very important as an effort to detect throat disorders objectively, safely and comfortably.

RESEARCH METHODOLOGY

The throat anatomically consists of the pharynx and larynx, superiorly starting at the base of the skull and nasopharynx, extending to the esophageal inlet and most proximally to the trachea. Throat disorders can mean irritation, itching, burning, or pain in the throat area. Additionally, from the patient's perspective, throat may refer to the entire pharynx and larynx, the soft tissues of the neck, or one localized area. Throat disorders can be a presenting symptom of a variety of different diagnoses. Most throat disorders are caused by viruses (Anthony, 2004).

One of the characteristics of infrared is that it is invisible (Wrotniak, 2020). Like electromagnetic waves, infrared waves have reflection, absorption and transmission properties that depend on the material they are exposed to. Infrared waves can be easily absorbed by various materials (Jewett, 2004). The radiation emitted by an object at room temperature is mostly in the infrared region. This shows that objects will easily emit infrared radiation so that using infrared thermography techniques is easier (Adhi, 2013).

Infrared thermography is a non-invasive and non-ionizing imaging technique for recording body surface temperature (Kevin Howell, 2020). Temperature is an excellent indicator of health, because changes of just a few degrees in the skin can be used as an indicator of possible disease (Jones, 1998). Thermal cameras are passive sensors that capture infrared radiation emitted by all objects with temperatures above absolute zero and describe the emission of infrared radiation (Rikke, 2014). The fact that radiation is a function of an object's surface temperature allows cameras to calculate and display this temperature. However, radiation measured with a camera not only depends on the temperature of the object, but is also a function of emissivity. Radiation also comes from the environment and is reflected by objects.

Some parameters and factors that influence images recorded with modern infrared camera systems are object emissivity, camera distance to object, object size, relative humidity, environmental temperature, external optical transmission, temperature range (ΔT), temperature range + level, color palette, wavelength range of the camera, observation angle, temperature dependence of emissivity, optical properties of material between the object and camera, use of filters, thermal reflection, wind speed, solar load, shadow effect of nearby objects, humidity, and thermal properties of the object (Vollmer, 2010).

In practical measurements with an infrared camera, the object emits radiation towards the camera where the object is focused on the detector and measured quantitatively. Infrared radiation detectors usually only within a limited bandwidth of the infrared spectrum, i.e. they mostly perform measurements in the two main IR bands: MWIR and

Indonesian Applied Physics Letters

LWIR. Systems that work in the NIR are tailored for specific applications only because the atmosphere tends to be opaque for that spectrum. The final result of the infrared system is a surface temperature map. Two-dimensional images are achieved by scanning mechanisms consisting of oscillating mirrors, or rotating refracting elements (such as prisms), which allow scanning of objects in both vertical and horizontal directions. Currently, new systems are based on staring focal plane array (FPA) technology. The overall performance of an IR imaging system is evaluated conventionally in terms of the useful and accurate information that can be obtained per unit of time, with several influencing parameters namely: thermal sensitivity or equivalent random noise level, frame rate or number of images per unit time, image resolution or the number of independent measurement data points on which the image is composed, the intensity resolution or the number of intensity levels that allow for small temperature differences. Thermal detectors convert the absorbed electromagnetic radiation into thermal energy which causes the temperature of the detector to rise. Then the electrical output of the thermal sensor is generated by a corresponding change in some physical property of the material (Meola, 2017).

This research was carried out based on systematic steps. At the data collection stage, the thermal sensor array image data is retrieved in digital form. Data collection was carried out at the Medical Instrumentation Laboratory, Department of Physics, Faculty of Science and Technology, Universitas Airlangga. The data collected is in the form of throat image data. The distance between the object and the camera is one meter then crop to get the region of interest only in the neck area. Data collection was carried out in the same room with the characteristics of a closed room, relatively close together so that the effects of shadows of nearby objects, thermal reflections, optical properties of the material between objects, and humidity had relatively the same values. The thermal camera used is a Caterpillar S60 thermal camera with White Hot mode, and the temperature range in the color palette is the same, namely 33°C to 38°C. In White Hot mode, objects that have a higher temperature are displayed in white and objects that have a lower temperature are displayed in black. This mode can also be used for detailed observations but keeps the display simple. The data obtained was divided into two groups, namely throat data that had no interference and throat data that contained interference.

The initial stage before image processing is determining good quality image data based on images captured by a thermal camera. Then, after sorting, the next stage is to group the data, namely images taken from people who have throat disorders (group A) and images taken from people who do not have throat disorders (group B). Next, the region of interest is selected so that an image is obtained only of the throat. Next, a threshold is carried out so that an image mapping is obtained that corresponds to the specified threshold value. then analyze and compare the suitability of the mapping results between throats that have disorders and those that do not have disorders based on the threshold values used. The results of mapping the throat that has problems are then used as a reference for analyzing test data.

The first stage in the software design scheme is data input from the thermal image. The next stage is cropping to obtain the Region of Interest (ROI) area. Next, the image in the throat area will be thresholded so that areas with gray levels above the threshold and those below the threshold are detected. Then the area that has a gray level above the threshold is compared with the total area of the ROI to determine whether there is a throat disorder.

RESULT AND DISCUSSION

This section contains several explanations regarding the detection of throat disorders from the results of thermal images of the neck using digital image processing. In this study, white hot mode was used because white hot mode is displayed in grey level form, where the gray level in the image is linear with temperature. When taking pictures, the minimum to maximum temperature range used on the camera is 33°C to 38°C. So by using greyscale equation we can find out the relationship between the degree of gray and the temperature to be sought.

$$greyscale = (T^oC - 30^oC)(255/10)$$

Throat image data was taken from 16 participants, namely 8 participants complained of experiencing problems with their throats, and 8 participants reported no problems at all with their throats. Data collection was carried out at the same distance, namely one meter, in the same place and at almost the same time. The Palatte color used has a temperature range from 33°C to 38°C, with a temperature of 33°C represented by black while a temperature of 38°C is represented by white, while temperatures between 33°C-38°C are represented by degrees of gray between 0-255. An example of a thermal image captured is shown in FIGURE 1.
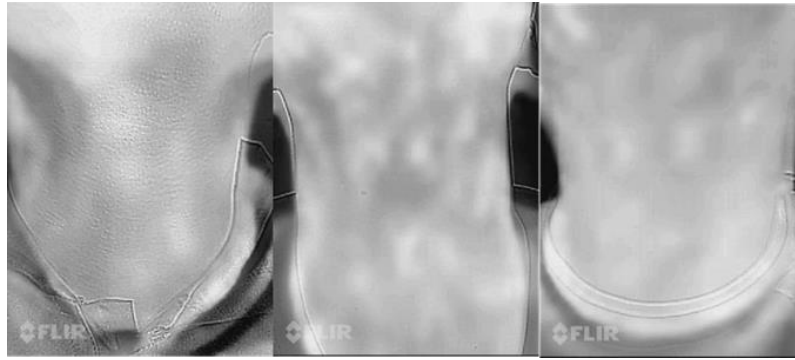
(a)
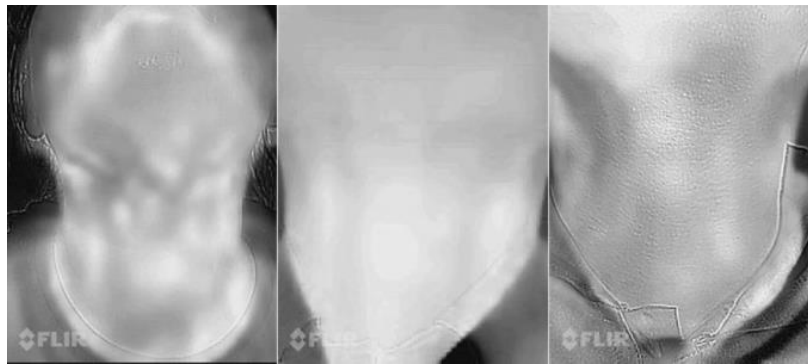
(b)

FIGURE 1. Thermal images of the throats of 3 participants who (a) reported no problems with their throats, (b) reported problems with their throats. .

TABLE 1. Questionnaire about perceived symptoms
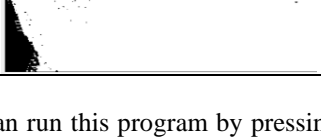
Object	Feeling itchy/uncomfortable in the area throat	Feeling pain in the throat area	Feeling pain/difficulty swallowing	Cough	Hoarseness	Burning feeling in the throat area
1	–	–	–	–	–	–
2	√	–	–	√	–	–
3	–	–	–	–	–	–
4	–	–	–	–	–	–
5	√	√	√	√	√	–
6	√	√	–	–	–	–
7	–	–	–	–	–	–
8	–	√	√	√	√	–

In terms of medical diagnosis, a person is said to have a throat problem even if they only experience one of the symptoms as in TABLE 1. And what the test taker filled in on the questionnaire was in accordance with the results of the diagnosis using the software, except for the 6th person who was identified as having a throat problem according

Indonesian Applied Physics Letters

to the software. questionnaire did not experience throat problems. This difference in results could be caused by environmental influences.

The preprocessing window is used to rotate, crop and scale images. Rotation is carried out so that the position of the object in the image can be upright so that data processing can be more accurate. then carry out the crop process in the crop menu to get the region of interest (ROI), namely the neck area. The image cropping process functions to obtain accurate information from the image by reducing unwanted components. Meanwhile, scale is used to adjust the image so that it has the desired size.

TABLE 2. Conversion results from greyscale images to binary images

Object	Binary Image	Percentage of White Color	Percentage of Black Color	Results
1.		26 %	74 %	no throat problems
2.		44%	56%	suffer from throat problems
3.		16%	84%	no throat problems
4.		23 %	77%	no throat problems
5.		44%	56%	suffer from throat problems
6.		49 %	51 %	suffer from throat problems
7.		0%	100%	no throat problems
8.		81 %	19%	suffer from throat problems

Users can run this program by pressing the load image button, then the selected image will be displayed. If the image is still not upright, making it difficult for the cropping process later, then we can rotate it according to our needs by setting it in the rotate column. We can crop the left, right, top and bottom of the image using the crop column.

Users can adjust the part they want to cut so that they only get the neck. And if you want to make the image size uniform, you can use the scale column. The conversion results from greyscale images to binary images are shown in TABLE 2.

The Processing window is used to further manage the image after the preprocessing stage. In the processing window there is a threshold column, which functions to convert the greyscale image into a binary image. Each pixel will automatically be matched to the existing threshold limit. If a pixel has a degree of gray above the threshold limit, then the color of that pixel will be converted to white. Meanwhile, if in a pixel, the gray degree value is less than the entered threshold limit, then in that pixel the color will be converted to black. After that, enter the limit value in the parameter set column. The limit in this case shows the minimum percentage of the area that is white, meaning if the white area is larger than the limit, meaning the throat is experiencing problems. If the white area is less than the limit, then the throat is identified as having no problems. After creating the software, the next step is to determine the threshold and limits for data testing.

Threshold determination is carried out using a trial error system to find the difference in area between the throat which is disturbed and which is not disturbed. Threshold search is carried out using software. The results found quite a visible difference at the threshold value of 190 or the equivalent of a temperature of 36.7°C. By using 3 normal throat data, it was found that the percentage of throat area that had a temperature above the threshold was 29%, 19%, and 37 %. Meanwhile, in the image of the throat that is disturbed, the percentage of areas that have a temperature above the threshold is 42%, 61%, and 39%. So a limit can be set at 38%, which means that if after thresholding, the white throat image is less than 38%, then the throat is identified as having no problems. And if the area of the white throat is more than 38% then the throat is identified as having a problem.

CONCLUSION

Throat disorder detection based on thermal images has been carried out using digital image processing. Image capture was carried out with the same color range on the camera, namely 33°C-38°C. The image obtained is then cropped to match the expected Region Of Interest. Next, threshold is carried out on the grey scale image with a threshold value of 190. Pixels that have a gray degree above 190 are converted to white, while those below the threshold are converted to black. Next, the percentage of each white and black area is calculated compared to the total area of the Region of Interest. If the percentage of the white area is greater than 38% compared to the area of the throat then it is identified as having a throat disorder, whereas if the percentage of white is less than 38% then it is identified as not having a throat disorder. Based on the detection that has been carried out, an accuracy rate of 87.5% was obtained using 8 test data.

REFERENCES

1. Catphones, https://www.catphones.com/download/User-Manuals/S60- Smartphone/S60-Panduan-pengguna-Bahasa-Indonesia.pdf, 2021.
2. M. A. M. Cristina, "Real-time tracking of self-reported symptoms to predict potential Covid-19", Nature Medicine, 26, 2020.
3. J. M. L. Feng, "Online Monitoring of Particle Temperature Using a Thermal Camera", Elsevier, 2020.
4. K. Adhi, "Pemeriksaan Kondisi Peralatan Mekanikal dan Elektrikal Gedung Menggunakan Metode Infrared Thermography", Jurnal Teknik Elektro, 2013.
5. S. Anthony, "Sore throats", Elsevier, 2004.
6. Y. S. Irianto, "Analisa Citra Digital dan Content Based Image Retrieval", Bandar Lampung: CV Anugerah Utama Raharja, 2013.
7. S. Jewett, "Physics for Scientists and Endineers", California: Thomson Brookscole, 2004.
8. F. B. Jones, "A Reappraisal of the Use of Infrared Thermal Image Analysis in Medicine", IEEE, 1998.
9. D. K. H. Kevin, "Thermal Camera Performance and Image Analysis Repeatability in Equine", Elsevier, 2020.
10. M. Vollmer, "Infrared Thermal Imaging", Germany: Wiley-VCH, 2010.
11. B. C. Meola, "Infrared Thermography Basics. Infrared Thermography in the Evaluation of Aerospace Composite Materials", in C. B. Meola, "Infrared Thermography Basics. Infrared Thermography in the Evaluation of Aerospace Composite Materials", 2017.
12. N. A. Kusumanto, "Pengelolahan Citra Digital Untuk Mendeteksi Obyek Menggunakan Pengolahan Warna Model Normalisasi RGB", Seminar Nasional Teknologi Informasi & Komunikasi Terapan 2011, 2011.

13. B. T. G. Rikke, "Thermal Cameras and Applications : A survey", Springer, 2013.
14. B. T. G. Rikke, "Thermal Cameras and Applications : A survey", Aalborg University Denmark, 2014.
15. E. E. K. Seydi, "The use of infrared thermal imaging in the diagnosis of deep vein", Elsevier, 2017.
16. S. Sumriddetchkajorn, & Y. Intaravanne, "Two Dimensional Fruit Ripeness estimation using thermal imaging", Proceedings of SPIE - The International Society for Optical Engineering. Thailand, 2016.
17. A. J. Wrotniak, "Digital Camera Infrared", http// Digital Camera Infrared.com, 2020.
18. J. M. Blackledge, "Digital Image Processing Mathematical and Computational Methods", in J. M. Blackledge, "Digital Image Processing Mathematical and Computational Methods", Chichester, West Sussex: Horwood, 2006.

The Characteristic of Polyester Concrete with Local Sand of East Borneo as Filter

Asti Lolita Dewi[1,b], Rifqi Aulia Tanjung[1,c], Gusti Umindya Nur Tajalla[1,d], Ade Wahyu Yusariarta Putra Parmita[1,a]

[1] Materials and Metallurgical Engineering Study Program, Kalimantan Institute of Technology, Balikpapan, Indonesia

[a]Corresponding author: adewahyu27@lecturer.itk.ac.id
[b]06181013@student.itk.ac.id, [c]rifqi.aulia@lecturer.itk.ac.id, [d]gusti.unt@lecturer.itk.ac.id

Abstract. Concrete is a mixture of coarse aggregate and fine aggregate mixed with water and cement as a binder and filler. The disadvantages of traditional concrete are that high water absorption causes low chemical resistance, low modulus of elasticity, low impact strength and a long hardening time to reach its maximum properties, namely 28 days. The solution to these shortcomings that is being developed for construction material applications is by using polymers as polymer concrete. In this research, polyester resin and sand aggregate were used as basic materials. Polyester resin is a type of thermosetting polymer that is widely used in various applications such as automotive parts, composites and construction because of its suitable processing characteristics and affordable price. Meanwhile, the sand used is local Kalimantan sand, where from the XRF and XRD test results, local Kalimantan sand is included in the silica sand type. This research varies the weight fraction of polyester resin used to determine its effect on polymer concrete characteristics such as porosity, water absorption, compressive strength, and macro observations. Variations in the polymer weight fraction used were 20%, 25% and 30%. Compressive strength testing was carried out at the age of 7 days of concrete. The results of the porosity test show that the average porosity of all variations is ± 0.5%. Meanwhile, the average value of water absorption for all fractions is 0.2%. And the highest average value of compressive strength in the 30% polyester resin weight fraction was 66.9 MPa. So it can be concluded that all variations meet SNI standards to become concrete materials.

ARTICLE INFO

INTRODUCTION

Geographically, Indonesia consists of approximately 17,504 islands, and three-quarters of Indonesia's territory is in the sea [1]. Because of Indonesia's vast territory, infrastructure is needed to support the community in its activities, such as bridges and toll roads [2]. There are many construction projects taking place in Indonesia, and they need good-quality materials. The material that is often used and plays an important role in good infrastructure development is concrete [3]. Concrete is the easiest construction material to find and is often used to produce it [4]. Concrete is basically a mixture consisting of coarse aggregate and fine aggregate, then mixed with cement and water to form a fine binder [5]. According to Mulyono [6], the weakness of Portland cement concrete is that it takes a long time, approximately 24 hours, to harden completely and takes 28 days to reach maximum strength. Nowakci [7], in that research, found the disadvantages of traditional concrete are high water absorption, low chemical resistance, low elastic modulus, low impact strength, and long hardening time to achieve maximum properties. So, innovations are needed for concrete manufacturing so that it has faster production times, stronger mechanical properties, and a long-lasting structure. To overcome some of the shortcomings of concrete in general, Albi's research [8] states that there is a new material consisting of aggregate and polymer resin binder, which is being developed for application as a construction material with properties that are superior to cement concrete in general [9].

In the realm of construction, polymers have emerged as versatile materials, finding extensive utility as adhesives and matrices within concrete structures. One notable innovation in this domain is polymer concrete, a relatively recent entrant that has garnered widespread adoption across various sectors. From road infrastructure to bridge construction, underground projects to surface refurbishments, polymer concrete has proven its mettle. Its superiority over traditional cement-based counterparts lies in several key attributes: heightened mechanical resilience, expedited drying and solidification processes, resistance against abrasion and environmental degradation, impermeability to water, and superior sound insulation. These advantages make polymer concrete an attractive choice for modern construction needs [10]. Among the different types of polymers, thermoset polymers are particularly prominent, offering superior strength, thermal endurance, and durability compared to thermoplastic alternatives [11]. In accordance with the Indonesian National Standard (SNI) 7833-2012 [12], concrete is mandated to possess a compressive strength of no less than 17 MPa. Previous investigations into polymer concrete have demonstrated compliance with this standard, showcasing an average compressive strength of 23.043 MPa [13]. This underscores the viability and robustness of polymer concrete as a construction material, meeting and even exceeding regulatory requirements.

Polyester resin, a quintessential thermoset polymer, plays a pivotal role in composite and construction applications due to its favorable processing characteristics and cost-effectiveness [14]. Polymer concrete formulations incorporating polyester resin exhibit commendable chemical resistance and structural integrity, making them suitable for a myriad of applications including fillers, piping materials, staircases, and fabrication components. The efficacy of polymer concrete hinges upon the composition and proportions of aggregates, as well as achieving a harmonious balance between aggregate constituents and resin content [15].

Furthermore, the utilization of locally sourced Kalimantan sand in this study as a constituent in polymer concrete blends aims to optimize mechanical and physical properties. This necessitates further investigations to delineate the ramifications of varying polyester volume fractions on the nuanced attributes of polymer concrete. By leveraging Kalimantan sand as a filler, the research endeavors to ascertain the optimal polyester resin volume fraction required to attain the desired mechanical and physical properties in polymer concrete formulations. This pursuit underscores a commitment to enhancing construction materials through empirical inquiry and innovation, catering to the evolving demands of contemporary infrastructure development and ensuring sustainability in construction practices.

METHODOLOGY

In this study, the characterization of polymer concrete is investigated through macroscopic observations, mechanical property analysis, water absorption, and porosity considering variations in the weight fraction of polyester resin. The study is divided into two main phases, namely the manufacturing process of polymer concrete samples and sample testing. The first phase involves the preparation of local Kalimantan sand by drying and sieving, as well as analysis using X-Ray Diffraction (XRD), X-Ray Fluorescence (XRF) techniques, and specific gravity measurement to identify the composition and physical characteristics of the sand. Subsequently, the composition of materials and resin is weighed according to the prescribed procedure before being homogeneously mixed in a single container. The mixture is then cast using a cylindrical mold with standard diameter and height, with lubrication applied to the mold for easy sample release after being allowed to stand for 24 hours at room temperature. After a 7-

day curing period at room temperature, the samples are macroscopically observed, and tests are conducted on compressive strength, porosity, and water absorption.

TABLE 1. Polymer Concrete Composition

No	%wt Polyester Resin	%wt Kalimantan Local Sand	Hardener
1	20%	80%	2%
2	25%	75%	2%
3	30%	70%	2%

RESULTS AND DISCUSSION

X-Ray Fluorescence Analysis

The results of XRF testing in Table 2 indicate that local sand from Kalimantan contains ten elements, with the highest mass percentage being silica (Si) at 96.8064%, followed by iron (Fe), aluminum (Al), and titanium (Ti). This finding is consistent with a previous study by Silvia [13], which also found that natural sand has the highest silica (Si) content at 81.7%, followed by iron (Fe) at 2.49%, calcium (Ca) at 14.8%, and several other elements with percentages of less than 1%, which can be considered impurities. Therefore, it can be concluded that this natural sand is silica sand due to the dominance of the Si element percentage in the XRF testing results.

TABLE 2. XRF test result

Element	Concentration	Unit	Line	Intensity	Judgment
Al	0.7450	wt%	Kα	58.87	---
K	0.0000	wt%	Kα	0.00	---
Si	96.8064	wt%	Kα	22055.77	---
Fe	1.0316	wt%	Kα	11289.10	---
Ti	0.7185	wt%	Kα	3505.02	---
S	0.2728	wt%	Kα	129.13	---
Ca	0.2269	wt%	Kα	517.98	---
Ni	0.1219	wt%	Kα	1557.03	---
V	0.0480	wt%	Kα	306.89	---
Cu	0.0289	wt%	Kα	387.21	---

X-Ray Diffraction Analysis

The XRD testing results of the local sand are depicted in Figure 1, showing similar findings to Hakim's study [16], where the peak intensity is highest at $2\theta = 26.59211°$. Additionally, Silvia's research [13] confirms this similarity, indicating that both the XRD curves of natural sand and local sand from Kalimantan exhibit the highest peak characteristic of quartz (SiO2) at $2\theta = 26.59°$. This alignment is further supported by XRF testing, which highlights the dominance of silicon (Si) in local Kalimantan sand, affirming its classification as silica sand.
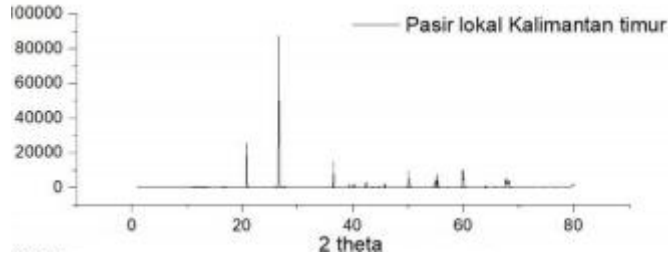
Indonesian Applied Physics Letters

FIGURE 1. XRD Test Results for Local Kalimantan Sand

Macro Observations

Macroscopic observations were conducted to visually examine the polymer concrete specimens using a digital microscope. The average pore sizes obtained from a 20% resin weight fraction were 0.36 mm, while those obtained from a 25% resin weight fraction were 0.37 mm. Increasing the resin content to 30% resulted in the absence of large pores, but some small pores were observed, as shown in Figure 4. These pores were assumed to be due to sand grains detached because the grain size ranged from 0.297 mm to 0.147 mm, rather than trapped air. All images (2, 3, and 4) exhibit white areas representing polyester resin and gray areas representing aggregates. However, black areas with irregular or round edges indicate the presence of pores [17].
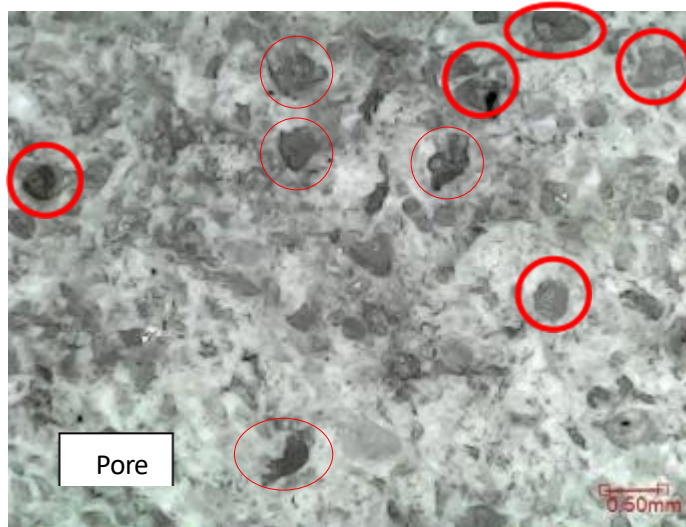

FIGURE 2. Results of macro observations of polymer concrete specimens with a weight fraction of 20% at 100X magnification

Indonesian Applied Physics Letters

FIGURE 3. Results of macro observations of polymer concrete specimens with a weight fraction of 25% at 100X magnification

FIGURE 4. Results of macro observations of polymer concrete specimens with a weight fraction of 30% at 100 X magnification

Porosity Analysis

Porosity can be defined as the ratio of pore volume to the total volume of the composite. The aim of this test is to determine the percentage of concrete pores relative to the total concrete volume. The data above are derived from calculations involving the mass of dry specimens, the mass of specimens weighed after being submerged for 24 hours, and the specimen volume. From Figure 5, the average porosity values were obtained: for a resin weight fraction of 20%, the average porosity percentage was 0.59%; for polymer concrete with a resin weight fraction of 25%, the average porosity percentage was 0.57%; and for polymer concrete with a resin weight fraction of 30%, the average porosity percentage was 0.52%. According to Tarigan [18], the porosity value for a resin weight fraction of 20% indicates a lack of molecular bonding in the polymer concrete, resulting in the formation of numerous pores. Additionally, the addition of resin leads to a reduction in porosity because the resin fills the pores and seals micro-defects in the polymer concrete [19].
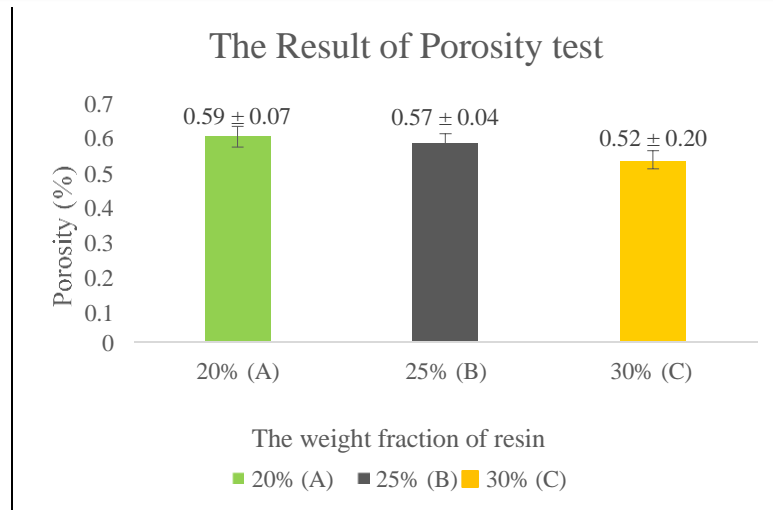
FIGURE 5. Graph of the relationship between porosity percentage and variations in weight fraction of polyester resin

Water Absorption Analysis

The data above are derived from calculations involving the mass of dry specimens and the mass of specimens weighed after being submerged for 24 hours. From Figure 6, the average values of water absorption testing are shown. For a resin weight fraction of 20%, the average water absorption percentage was 0.27%; for polymer concrete with a resin weight fraction of 25%, the average water absorption percentage was 0.24%; and for polymer concrete with a resin weight fraction of 30%, the average water absorption percentage was 0.19%.

Water absorption in concrete decreases as the polymer content increases, attributed to the pore-blocking effect of polymer particles [19]. Additionally, polymers are water-resistant materials, so polymer particles distributed within the concrete pores hinder water from penetrating through the concrete particles. With the addition of a resin weight fraction of 30%, the minimum water absorption value obtained was 0.19%, as the resin acts as a binder, reducing the pores in the polymer concrete. A lower water absorption percentage indicates higher quality polymer concrete [20].
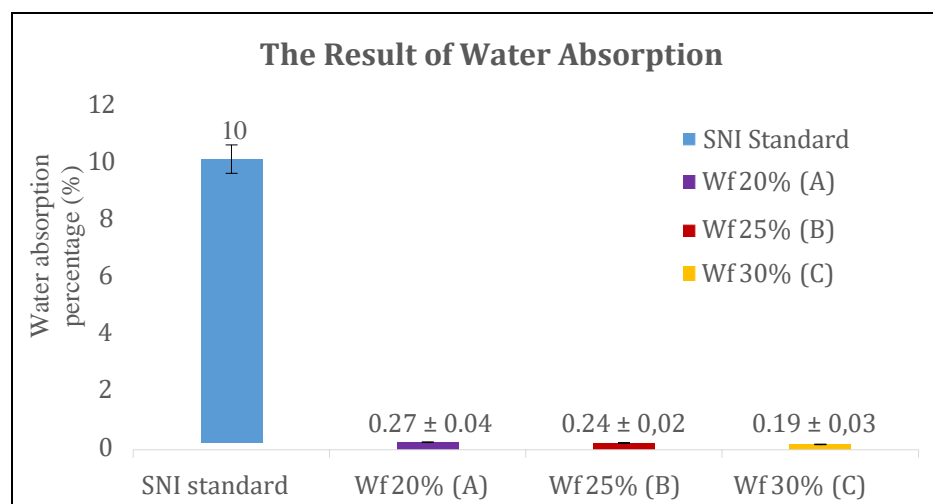

FIGURE 6. Graph of the relationship between the percentage of water absorption and variations in the weight fraction of polyester resin

Compressive Strength Analysis

The purpose of this test is to determine the concrete's ability to withstand compressive forces per unit area of concrete surface. The test was conducted on cylindrical polymer concrete samples with polyester resin weight fractions of 20%, 25%, and 30% at a testing age of 7 days. From Figure 7, the average values of compressive strength testing are shown. For ordinary cement concrete, the average compressive strength value obtained was 18.45 MPa. However, for polymer concrete with a 20% resin weight fraction, the average compressive strength value was 56.96 MPa; for polymer concrete with a 25% resin weight fraction, it was 60.76 MPa, and for polymer concrete with a 30% resin weight fraction, it was 66.9 MPa. The increase in resin percentage enhances the bonding between resin and aggregate, as polyester resin acts as a binder to bind aggregates and fill the interparticle voids, thus reducing the pores in the concrete [21]. This is supported by macroscopic observations, porosity testing, and water absorption testing, where an increase in resin content results in resin covering the pores or voids of the polymer concrete specimens, leading to stronger bonding between sand particles and resin, thus increasing the compressive strength. The lowest strength value was obtained with a 20% resin weight fraction, as a reduction in resin weight fraction can cause an increase in pores in the polymer concrete [19].
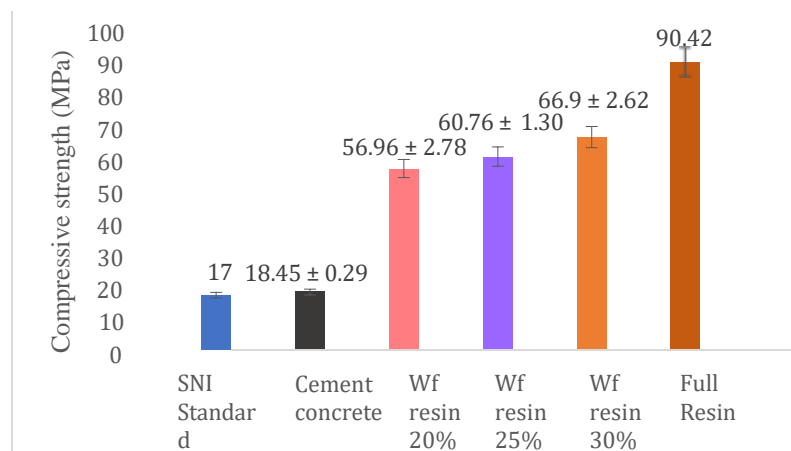

FIGURE 7. Graph of the relationship between compressive strength and variations in the weight fraction of polyester resin in polymer concrete

CONCLUSION

The conclusion drawn from this research is the successful production of polymer concrete, as evidenced by the testing results surpassing the average SNI standards for all variations of polymer concrete. The most optimal material is found in polymer concrete with a 30% polyester resin weight fraction, exhibiting the lowest porosity value at 0.52%, the lowest water absorption value at 0.19%, and the highest compressive strength at 66.9 MPa. Macroscopic testing of specimens with a 30% resin content reveals that polyester resin uniformly coats the aggregate, consisting of sand, resulting in the nearly imperceptible presence of pores.

ACKNOWLEDGEMENT

REFERENCE

1. Lasabuda, Ridwan. Pembangunan Wilayah Pesisir dan Lautan Dalam Perspektif Negara Kepulauan Republik Indonesia. *Jurnal Ilmiah Platax*, Vol.1- 2, ISSN: 2302-3589 (2013)
2. Abizandika, Hazdhika, Hari Wibisono, dan Sempurna Bangun. Perencanaan Ulang Jembatan Tukad Bangkung Kabupaten Badung, Bali Dengan Metode Cable Stayed. *Jurnal Sains dan Teknologi Utama*, Volume XI, Nomor 3 (2016)

3. Helmi, Risyaf Pratama. Analisis Lentur Balok-I Prategang Dengan Variasi Luas Flens Bawah. Diploma thesis, Universitas Andalas (2021)

4. Supriatna Indra. Kajian Beton PolimerMenggunakan Bahan Campuran PerekatResin (kadar 30%) Serta Penambahan *Fiberglass* dengan Kadar Bervariasi Terhadap Kuat Tekandan Kuat Tarik Belah Beton. Bandung : Universitas Sangga Buana (2020).

5. Adi, Prasetya. Kajian Jenis Agregat dan Proporsi Campuran Terhadap Kuat Tekan dan Daya Tembus Beton Porus. Jurnal Teknik Vol.3 No.2 Jurusan Teknik Sipil, Fakultas Teknik, Universitas Janabadra, Yogyakarta (2013)

6. Mulyono T. "Teknologi Beton". Penerbit Andi Yogyakarta (2004)

7. Nowacki Bartlomiej, Degirmenci Berk, Tekeli Dogus Berke and Smolen Jakub. Mechanical Properties of Polymer Concretes Based On Unsaturated Polyester Resin Reinforced With Milled Car Windscreen Waste Glass and Quartz Sand. Polish Society of Composite Material. ISSN: 2084-6096 (2021)

8. Albi, Ifrah, "Pembuatan dan Karakterisasi Betonn Polimer dengan Agregat Batu Apung serta Serat Kulit Jengkol sebagai Filler", Universitas Sumatera Utara : Medan (2019)

9. Torkittikul P, Nochaiya T, and Chaipanich A. The Investigation of Polyester Resin Polymer Concrete with Various Amount of Cinstruction Aggregate. Thailand (2020)

10. Choi, Y. W., D. J. Moon, J. S. Chung, S. K. Cho. 2015. Effects of waste PET bottles aggregate on the properties of concrete. Cement Concr Res. Vol. 35 : 776-781 (2015)

11. Callister Jr, W. D., & Rethwisch, D. G. Fundamentals of Materials Science and Engineering. John Wiley & Sons, Ltd (2014)

12. Badan Standarisasi Nasional. Standar Nasional Indonesia 7833. 2012. Tentang Cara Perancangan Beton Pracetak dan Beton Prategang Untuk Bangunan Gedung. Jakarta (2012)

13. L. Silvia and M. Zainuri. "Analisis Silika (SiO_2) Hasil Kopresipitasi Berbasis Bahan Alam menggunakan Uji XRF dan XRD," J. Fis. dan Apl.,vol. 16, no. 1, p. 12 (2020)

14. Surya, I dan Suhendar. Sifat Mekanis Komposit Serat Acak Limbah Sabut Kelapa Bermatriks Polyester Resin (2016)

15. Shakil Ahmed Usaid and Hassan Abu Bin. Behavior and Properties of tin slag Polyester Polymer Concrete Confined with FRP Composite Under Compression. Journal of The Mechanical Behavior Materials. Universitas Teknologi Malaysia (2020)

16. Hakim Luqman, Dirgantara Made, Nawir Muhammad. Karakterisasi Struktur Material Pasir Bongkahan Galian Golongan C Dengan Menggunakan X-Ray Difraction (X-RD) Di Kota Palangkaraya. Universitas Palangkaraya (2019)

17. Shakil Ahmed Usaid and Hassan Abu Bin. Behavior and Properties of tin slag Polyester Polymer Concrete Confined With FRP Composite Under Compression. Journal of The Mechanical Behavior Materials. Universitas Teknologi Malaysia (2020)

18. Tarigan, Shiamny Nur Khair. Pembuatan dan Karakterisasi Bton Polimer dari Serat Tandan Kosong Kelapa Sawit dan Cangkang Telur dengan Resin Polyester. Universtas Sumatera Utara (2019)

19. Supriatna Indra. Kajian Beton Polimer Menggunakan Bahan Campuran Perekat Resin (kadar 30%) Serta Penambahan Fiberglass dengan Kadar Bervariasi Terhadap Kuat Tekan dan Kuat Tarik Belah Beton. Bandung : Universitas Sangga Buana (2020)

20. Siregar, Diego Van Castro. "Karakterisasi Beton Polimer Dari Agregat Pasir Dan Batu Apung Serta Serat Tebu Dengan Resin Epoksi". Medan: Univeristas Sumatera Utara (2017)

21. Torkittikul P, Nochaiya T, and Chaipanich A. The Investigation of Polyester Resin Polymer Concrete with Various Amount of Cinstruction Aggregate. Thailand (2020)